Environmental Science & Technology, Volume 59, Issue 3, pp. 1844-1853
DOI:10.1021/acs.est.4c13849

Targeted Enrichment of Nucleic Acid Bionic Arms Enhance Hydrolysis Activity of Nanozymes for Degradation and Real-time Monitoring of Organophosphorus Pesticides in Water

Jialong Zhou,[1] Dinghui Xiong,[1] Hu Zhang,[1] Jiaxuan Xiao,[1] Rui Huang,[1,2] Ze Qiao,[1,2] Zhugen Yang[2]* and Zhen Zhang[1]*

[1] School of the Environment and Safety Engineering, Jiangsu University, Zhenjiang, 212013, China

[2] Faculty of Engineering and Applied Sciences, Cranfield University, Milton Keynes MK43 0AL, UK

*Corresponding author:

E-mail: zhugen.yang@cranfield.ac.uk, zhangzhen@ujs.edu.cn

Fax: +86-511-88790955

ABSTRACT: Organophosphorus pesticides (OPs) pose significant environmental and health risks, and their detoxification through catalytic hydrolysis using zirconium-based metal–organic frameworks (Zr–MOFs) has attracted considerable interest due to the strong Lewis acidic metal ions. Albeit important, the defects of the materials for OPs hydrolysis (e.g., poor degradation efficiency, rate and selectivity) limit their further application. Herein, a nucleic acid bionic arms modified biomimetic nanozyme (MOF-808-Apt) was designed through Zr–MOF and specific aptamer against OPs, which was employed for efficient and selective degradation of OPs. At the system, the functionalized biomimetic nanozyme can continuously capture trace OPs onto its catalytic sites for degradation with the fabricated nucleic acid bionic arms, significantly improving their catalytic activities compared to bare MOF-808 using paraoxon as a model of OPs, providing better performances including (i) excellent degradation efficiency, boosting from 4% to over 60% within 6 minutes; (ii) satisfactory catalytic rate, and the pseudo-first-order-rate constants of paraoxon hydrolysis improved from 0.09 to 0.14 min^{-1}; (iii) good selective degradation because of aptamers used. Besides, this dynamic degradation process could be visually recorded in real time with high sensitivity (limit of detection, 0.18 μM) because of the obvious color change of reaction solution, and signal amplification ascribed to increasing local concentrations of targets by the nucleic acid bionic arms. Summarily, this work provides a new strategy for effective and selective degradation of typical OPs, and concurrently monitoring their dynamic degradation process.

KEYWORDS: metal–organic framework, nanozyme, signal amplification, rapid detection, organophosphorus pesticides

Published by American Chemical Society. This is the Author Accepted Manuscript issued with: Creative Commons Attribution License (CC:BY 4.0).
The final published version (version of record) is available online at DOI:10.1021/acs.est.4c13849. Please refer to any applicable publisher terms of use.

INTRODUCTION

Organophosphorus pesticides (OPs) are popularly used for effective pest control in modern agricultural production because of their low cost and high efficacy,[1-3] representing approximately 38% of the total pesticides market[4]. However, OPs are antiacetylcholinesterases and act via a common mechanism of phosphorylation of acetylcholinesterase (AChE), which will disable AChE to catalyze acetylcholine, and result in cholinergic toxicity against aquatic organisms due to over acetylcholine accumulation.[5-8] Considering that extensive usage of the chemicals could bring about serious water eco-environment threats,[9, 10] their detoxification is urgently needed through degradation.

Organophosphorus hydrolases (OPHs) were identified as the key microbial enzymes for effective destruction of OPs.[11, 12] Even so, their catalytic performance could easily be influenced by some environmental stimuli, including temperature, pH and metal ions,[13, 14] suggesting its inadequacy for OPs degradation at real environments. As an alternative, hydrolytic nanozymes, an emerging class of nanoengineered artificial enzymes, offer significant advantages over natural enzymes in terms of stability, activity, cost, and scalability.[15-17] Wherein, zirconium-based metal-organic frameworks (Zr–MOFs) have been demonstrated of outstanding catalytic performance for detoxifying organophosphate agents in basic solutions, rapidly hydrolyzing OPs and significantly reducing their danger.[18-20] Especially for MOF-808, it exhibits the fastest hydrolysis catalytic rates for organophosphorus compounds compared to other materials.[21-23] Nevertheless, the defects of MOF-808 limited wide applications as (i) lacking recognition binding sites similar to those of natural enzymes; (ii) poor binding interactions at the catalytic interfaces.[24, 25] Consequently, trace amounts of OPs in environmental water struggle to reach the necessary concentration near the catalytic sites ("molarity effect") for effective hydrolysis.[26, 27] Additionally, various non-target pollutants may block and occupy the pores and active sites of nanozymes, resulting in a loss of catalytic activity.[28] Therefore, the development of a versatile method to concentrate target substrates while simultaneously blocking non-target contaminants would be a promising strategy for Zr–MOFs-based OPs hydrolysis.

Aptamers are sequence-specific nucleic acids selected through the systematic evolution of ligands by exponential enrichment (SELEX) procedure.[29] They show unique characteristics of high affinity and selective binding properties towards low-molecular-weight ligands and macromolecules,[30-32] which can be employed to improve the selectivity of Zr–MOFs.[33] Taking advantage of the excellent selectivity and binding affinity of aptamers for OPs, conjugating ligand-binding aptamers to nanozymes may provide a potential means to improve the performance of nanozymes.[24, 34]

In this work, an effective hydrolytic nanozyme (MOF-808) was modified by specific aptamers against OPs, which provided unique bionic arms to concentrate ligand-substrate complexes at catalytic sites, while blocking non-target substrate interference, significantly improving the specificity and catalytic activity of MOF-808 in water pollution control, and solving the shortcomings of traditional nanozymes in real water environment application. More importantly, the color change of the reaction solution was observed when paraoxon (a model from three investigated OPs) was being hydrolyzed, which could be used as a new signal amplification strategy for real-time monitoring of OPs in waters.

EXPERIMENTAL SECTION

The details regarding the reagents, instruments, preparation methods for materials, characterization methods, degradation procedures, aptamers experimental procedures, kinetic measurements, and analytical methods were provided in the Supporting Information.

RESULTS AND DISCUSSION

Synthesis and Characterization of MOF-808/Apt and MOF-808-Apt. MOF-808 and MOF-808-NH_2 were synthesized via a solvothermal method, employing H_3BTC or H_2BTC-NH_2 as ancillary ligands to competitively coordinate with the Zr_6 cluster.[35] The broad-specific aptamers of OPs were absorbed onto MOF-808 (Figure 1A, a) or covalently bound with MOF-808-NH_2 (Figure 1A, b) to obtain MOF-808/Apt and MOF-808-Apt products, respectively. Seen in Figure 1B by scanning electron microscopy (SEM), MOF-808/Apt and MOF-808-Apt possessed an octahedral morphology, verifying the overall morphology was not changed after the combination of aptamers. In addition, the digital light scattering analysis revealed that MOF-808 and MOF-808-NH_2 possessed average hydrodynamic diameters of 689.3 nm and

862.8 nm, respectively (Figure 1B). Meanwhile, according to the elemental mappings based on energy dispersive X-ray spectroscopy (EDS), an even distribution of the elements C, O, Zr and P were found in MOF-808/Apt, while C, N, O, Zr and P in MOF-808-Apt (Figure 1C). As shown in FT-IR spectroscopy, no obvious bands corresponding to the free carboxyl groups were observed at 1730–1710 cm^{-1}, together with the presence of Zr–(μ_3)O bond peaks at 645 cm^{-1} and 756 cm^{-1}, confirming the bidentate coordination between Zr^{4+} and the carboxyl in the ligand, which is the character of MOF-808 based MOFs (Figure 2C).[36] The nitrogen physisorption isotherms of pristine MOF-808 and defective MOF-808-NH_2 showed typical type I of the IUPAC classification respectively with surface areas of 1856 m^2/g and 3049 m^2/g, indicating that the highly microporous structure of MOF-808 was maintained (Figure 2D).[37] Besides, the significant increase in nitrogen uptake can be correlated to the formation of defective sites caused by defect inducers in the framework.[38] Additionally, the average pore size of MOF-808 was around 16.8 Å while that of defective MOF-808-NH_2 was slightly increased to 18.7 Å (Figure S1).

Figure 2A presented the PXRD patterns of MOF-808, MOF-808-NH_2, MOF-808/Apt and MOF-808-Apt, which revealed the great agreement in characteristic peaks of the several MOFs, indicating the intrinsic crystalline structure of catalysts was not affected by the modification of aptamers. To further examine the chemical state of elements in the produced MOFs, X-ray photoelectron spectroscopy (XPS) was employed, and the results of elements presence were consistent with those of EDS (Figure 2B). Meanwhile, the high-resolution XPS spectrum of the additional P 2p signal demonstrated the existence of aptamers (Figure S2). Furthermore, Figure S3 displayed the high-resolution XPS spectrum of N 1s, which can be detected as a dominant C–N binding energy of 399.36 eV and the binding energy of 398.37 eV corresponds to the formation of C=N, providing the evidence for the covalent conjunction of the aptamer on MOF-808-NH_2 through Schiff base reaction. Additionally, FT-IR spectroscopy was further used to investigate the coordination reaction between MOFs and aptamers, and Figure 2C indicated that the P–O stretching vibration peak (1105 cm^{-1}) appeared in the aptamers modified Zr–MOFs, implying that the bands at 1256 and 1221 cm^{-1} were obviously enhanced in MOF-808-Apt, corresponding to the C–N and C=N stretching vibration, which thus illustrated the covalent conjunction of aptamers onto MOF-808-NH_2 by glutaraldehyde. The nitrogen

adsorption−desorption isotherm of aptamers modified Zr-MOFs at 77 K were further performed (Figure 2D). After functionalization with DNA, the specific surface area of MOF-808/Apt and MOF-808-Apt respectively decreased to 1543 m^2/g and 2661 m^2/g, suggesting that aptamers modification may block some of the pores.[39] Zeta potentials were also measured to prove the presence of DNA on the surface of Zr-MOFs, as summarized in Figure 2E, after the modification with negatively charged aptamers, the zeta potential of MOF-808-Apt decreased from 35.1 mV to –4.8 mV and MOF-808/Apt decreased to 7.3 mV. Meanwhile, polyacrylamide gel electrophoresis was utilized to further verify the successful construction of the aptamers modified biomimetic nanozymes (Figure 2F). Compared with the bright band of initial concentration of aptamers (Lane 1), the bands of residual aptamers after modifying MOF-808 and MOF-808-NH_2 were shallower (Lane 3 and Lane 4), representing that different amounts of aptamers were successfully decorated onto the Zr–MOFs surface. By comparison with MOF-808-Apt, MOF-808/Apt showed the partial detachment of aptamers from MOF-808 surface after reacting with the targets (Lane 7 and Lane 8), demonstrating the robust link between aptamers and Zr–MOFs by Schiff base bond. All of these results confirmed that the broad-specific aptamers had been successfully attached to the MOFs.

Selective Degradation of OPs. To elucidate the activation procedures and hydrolysis efficiency of these biomimetic catalysts, MOF-808 and its derivatives were utilized as mimics for OPH for the degradation of OPs because the relatively low node connectivity of the Zr_6-based nodes (6-connected) results in a large number of Lewis acidic active sites available for catalysis to occur.[40] Momeni et al. examined hydrolysis in MOF-808 computationally and found that, in addition to enhanced accessibility to the Zr_6 node, a favorable H-bonding interaction between the μ_3–OH on the 6-connected Zr_6 node and the attacking water molecule could potentially contribute to the observed rapid catalytic hydrolysis.[41] In addition, the hydrolysis seems to occur with the nucleophilic attack of the organophosphorus by aqueous hydroxide ions, reactions are typically conducted at alkaline pH values to ensure a sufficient amount of hydroxide ions present.[22, 40]

Inspired by enzymatic hydrolysis catalysts found in nature, the possible mechanism of Zr–MOFs-based organophosphorus hydrolysis catalysts labelled with aptamers is proposed (Figure 3A). Firstly, the aptamers are employed as bionic arms that can specifically identify

and actively bind the target substrates to the place near the active sites of Zr–MOFs. Then, coordination of the organophosphorus substrate to the Zr(IV) active sites occurs through the phosphoryl oxygen.[21] With enough alkalinity of the solvent, the μ_3–O hydrogen is absorbed by the base.[40] Unlike the bridging hydroxide in natural enzymes, the bridging μ_3-oxo in the Zr_6 node remains intact, and nucleophilic attack on the organophosphorus substrate occurs from a water molecule into solution.[40] Finally, the leaving group is eliminated, and catalytic turnover of anionic products occurs with the replacement of one aqua and one hydroxo ligand on the Zr_6 node.[21]

In a follow-up experiment, typical OPs containing different ester bonds (e.g., –OP=S and –OP=O) were chosen to further verify their rapid and efficient degradation by the fabricated biomimetic nanozymes, which was analyzed using high-performance liquid chromatography-mass spectrometry (HPLC-MS) (Figure S4–6). Meanwhile, the hydrolysis product of the reaction was observed and the insight into the atomic-scale mechanism for coordination and hydrolysis of an organophosphorus substrate was provided (Figure S7). Firstly, MOF-808 with organophosphorus hydrolase activity were implemented to catalyze the hydrolysis of paraoxon, profenofos and isocarbophos. As shown in Figure 3B–D, the degradation rates against the three OPs were respectively 4.00%, 94.40% and 94.57%, indicating that MOF-808 had certain hydrolysis effects. The degradation rates of MOF-808-NH_2 for the three OPs were 11.86%, 97.27% and 98.61%, respectively, suggesting that the performance of MOF-808-NH_2 was slightly enhanced because of the defect engineering, in which defect-induced active have been reported to play an important role.[36, 42] As exhibited by Figure S8, MOF-808-NH_2 showed the obvious peaks with higher intensities at g = 2.003, indicating the presence of O-vacancies in the network frameworks.[43, 44] Additionally, Raman spectroscopy demonstrated the enhanced characteristic peaks at 1006 cm^{-1} and 1073 cm^{-1}, as well as the new band at 3269 cm^{-1} emerged in MOF-808-NH_2, both suggesting the presence of defects (Figure S9).[45-48] Meanwhile, the amino groups impact subtle changes on the microsolvation environment around the active sites on the Zr_6 nodes, ultimately resulting in increased nucleophilicity of water molecules for attacking the organophosphorus substrate coordinated to the Zr_6 node.[21, 42] Then, similar evaluations were also employed using MOF-808/Apt. Seen in Figure 3B–D, benefiting from the targets recognition and capture by aptamers, the degradation rates of the three OPs using

MOF-808/Apt were respectively increased by 14.47%, 4.15% and 4.72%. According to the Michaelis–Menten model, the first-order rate constant of paraoxon for MOF-808 and MOF-808/Apt were 0.09 min^{-1} and 0.11 min^{-1}, meaning that the hydrolytic capability of MOF-808/Apt was improved, but not so obvious, potentially ascribed to that the aptamers adsorb via electrostatic adsorption lacked sufficient stability, since aptamers modified MOF-808 would be desorbed due to electronegativity or conformational change during the process of targets recognition (Electrophoresis Lane 7). Under the same conditions, the degradation rates of the three OPs were significantly improved by MOF-808-Apt, with respective increase of 60.95%, 5.40% and 5.30% (Figure 3B–D), and the corresponding first-order rate constant of paraoxon for MOF-808-Apt reached 0.14 min^{-1} excitingly, which was attributed to the stable combination of aptamers and MOF-808-NH_2 through Schiff base linkages with the aldehyde group on glutaraldehyde. Additionally, since the 3′ end of the aptamer was linked onto MOF-808-NH_2 through an octyl linker, the whole aptamers were more flexible on the surface of MOF-808-NH_2 instead of curling up around the central cell, which is beneficial for the exposure of aptamers for the binding of targets.[33] Thus, a higher local substrate concentration can be obtained around the nanozyme catalytic sites, depending on the stable identification and effective capture by nucleic acid bionic arms, which accounts for its superior catalytic ability than that by bare Zr–MOFs.

Besides, PNPP was applied as a model compound with low toxicity, representing widely used nitro-group containing organophosphates in aqueous medium, and its structure is slightly different from that of OPs commonly used.[49, 50] Interestingly, contrary to the performance in OPs hydrolysis, both of the aptamer-modified nanozymes MOF-808/Apt and MOF-808-Apt displayed obviously declined catalytic capability compared to MOF-808 and MOF-808-NH_2 in the hydrolysis of PNPP. Compared with the degradation rates of MOF-808 for PNPP, the degradation rates of MOF-808/Apt and MOF-808-Apt for PNPP decreased by 13.74% and 11.06%, respectively (Figure 3E). It could be speculated that the conjugated aptamers spatially hindered the interfering molecules from accessing the catalytic sites on the Zr–MOFs.

All the above results indicated that nucleic acid bionic arms modified nanozymes not only greatly improve the catalytic effect on targets, but also effectively prevent non-specific substances from approaching the catalytic sites, thereby reserving more active sites for the

efficient catalysis of target substrates. This property provides a possibility for biomimetic nanozymes to achieve efficient removal of specific types of pollutants from complex waters, which is of great significance for real water treatment applications.

Mechanism of Aptamers Modified Zr–MOFs with Enhanced Phosphatase-like Activity. The aptamer-modified Zr–MOFs show enhanced phosphatase activity in part due to the broad-specific aptamers that can bind to a specific class of OPs targets with high affinity.[33, 51] To determine the different affinities of the broad-specific aptamers to different kinds of typical organophosphorus compounds, a binding assay was performed by competitive inhibition (Figure 4A). The stronger the binding affinity between the aptamers and the targets, the fewer aptamers bound to the molecular beacon, resulting in less molecular beacon fluorescence turned on and showing a higher inhibition rate. Based on which, a series of structurally similar compounds were examined, including three typical OPs (paraoxon, profenofos and isocarbophos) and PNPP. As shown in Figure 4B and 4C, the aptamers used displayed the highest binding affinity against paraoxon with inhibition ratios of over 75%, and above 50% against the other two OPs. In contrast, extremely low inhibition ratios (below 10%) were observed in binding PNPP. These results suggested that the broad-specific aptamers could bind to a class of typical OPs with higher specificity. In addition, the circular dichroism (CD) spectra of the broad-specific aptamers all contained positive peaks at 281 nm and a negative peak at 248 nm. As displayed in Figure S10A–C, the positive peak at 248 nm shifted to 252 nm upon the addition of target substrates, which indicated that the broad-specific aptamers underwent a conformational change after binding to three OPs.[52, 53]

Moreover, CD also be employed to further assess the structural responses of aptamers fixed to the surface of MOFs. Figure S10D–F demonstrated that after binding with the targets, the peak value at the corresponding position in the chromatogram showed similar changes to those observed in previous results. This suggested that the behaviors of aptamers were not affected after the construction of Zr–MOFs-Apt, and their structural changes were consistent with those observed during the detection of the three detected OPs, thereby proving that the heterogeneous surface did not interfere with the aptamer affinity. To further confirm that the improved catalytic activity of biomimetic nanozymes was due to the active grabbing by aptamers with secondary structures on the material surface, the poly(A), poly(C), poly(T) and random DNA

chains were modified onto Zr-MOFs surface to compare with the aptamers modified Zr-MOFs (Figure 4D and S11). Interestingly, contrary to the significant enhancement of the catalytic activity by aptamers against OPs, modification of poly(A), poly(C), poly(T) and random DNA chains all had an inhibitory effect on the catalytic activity. This result also suggested that the changes of physical properties caused by nucleic acids, such as electronegativity (Figure 2E) and hydrophobicity (Figure S12) changes, did not play the key role in the enhancement of catalytic activity. Meanwhile, as displayed in Figure S13, the catalytic activity of MOF-808-Apt was significantly reduced toward paraoxon under extreme conditions, such as strong alkali (pH > 10) and high temperature (T > 70°C), which was hypothesized that the aptamers lost their binding ability due to hydrogen bond break or conformational change under strong alkali or high-temperature conditions. Hence, the long single-chain structure might be attached to the material surface to shield the active sites, and had a blocking effect on all substances including the targets, resulting in a decrease in the overall activity of biomimetic nanozymes.[39, 54] In summary, these results proved that it was aptamers that play the role of bionic arms on the material surface, realizing active grasping of the specific target object and hindrance of non-target objects. More importantly, the conjugation of aptamers to the heterogenous catalytic interfaces adds a functional selective binding dimension to the hybrid catalyst emulating enzyme functions.[26, 55]

Subsequently, the substrate affinities of Zr–MOFs with or without nucleic acid bionic arms was investigated by enzyme kinetics theory and methods using paraoxon as a substrate (Figure S14). Wherein, apparent kinetic parameters of MOF-808, MOF-808-NH_2, MOF-808/Apt and MOF-808-Apt were obtained by the double reciprocal of the Michaelis-Menten equation. Initial reaction rates of four nanozymes were calculated and applied to the double reciprocal of the Michaelis-Menten equation, $1/v = (K_m/V_{max})\cdot(1/[s]+1/Vmax)$.[56] As shown in Figure S15, the K_m and V_{max} of four nanozymes were obtained from Lineweaver-Burk plots. The K_m of MOF-808, MOF-808-NH_2, MOF-808/Apt and MOF-808-Apt for paraoxon were 1.352, 0.904, 0.76 and 0.297 mM, respectively. In addition, the apparent K_m value for nucleic acid bionic arms modified Zr–MOFs was about 1.5-3 times smaller than that of bare Zr–MOFs, and was much smaller than nanozymes that mimic OPH in other studies (Table S2). Since the chemical reactions occur mainly on the surface of nanozymes, thus the smaller K_m values of nucleic acid

bionic arms modified nanozymes could be attributed to the cluster of active-site–binding site constituents, which would enrich the target substrates to active sites. In comparison with bare Zr–MOFs, the nucleic acid bionic arms modified nanozymes (MOF-808/Apt and MOF-808-Apt) showed higher affinity towards the target substrate paraoxon, which indicated that attaching aptamers to the MOFs surface did not deactivate the catalytic sites, and reduced distance between the substrates and the active sites for promoting the catalytic process.[24, 53]

In conclusion, the enhanced phosphatase activity of the modified Zr–MOFs benefits from the high affinity of aptamers, which allows them to actively recognize and bind the targets; on the other hand, it comes from the cluster formed by the combination of aptamer and nanoparticle core, which significantly improves the affinity between biomimetic nanozymes and target substrates, enabling a large number of target substrates to be enriched at the active sites of MOFs for effective hydrolysis.[26, 27]

Colorimetric Assay for Paraoxon Detection. Due to the important role in recognition, capture and enrichment played by nucleic acid bionic arms, paraoxon can be rapidly degraded by these biomimetic nanozymes to produce yellow product p-nitrophenol (p-NP), and realize an amplified colorimetric signal with the characteristic absorption peak of UV-vis spectra at 400 nm, based on which, a biosensor for paraoxon was designed (Figure 5A). In light of this, the constructed biomimetic nanozymes can not only quickly catalyze OPs for selective degradation, but also can be used as a sensing platform for sensitive detection of OPs, which serves as a nanoreactor that integrates the function of degradation and detection together.

As shown in the UV-vis spectra (Figure 5B), individual paraoxon, aptamer, MOF-808, MOF-808-NH_2, MOF-808/Apt and MOF-808-Apt did not show absorption peaks at 400nm. The similar phenomena appeared when aptamers were mixed with paraoxon, indicating that bare aptamers only served to identify and capture the targets without exhibiting catalytic activity for paraoxon hydrolysis. In contrast, obvious characteristic absorption peaks at 400 nm emerged in the UV-vis spectra after addition of a series of aptamers-modified Zr–MOFs, suggesting that the element Zr may play a crucial role in catalyzing the hydrolysis of paraoxon.

MOF-808-Apt was selected as the most suitable material for colorimetric assay for conducting a colorimetric assay for paraoxon. Shown as Figure 5C, the characteristic absorption peak at 400 nm was gradually intensified as the concentration of p-NP increased

from 0 to 300 μM, when the wavelength was scanned from 300 to 500 nm. Simultaneously, the solution increasingly turned yellow. Under the optimal conditions (Figure S16), using the fitting equation A = 0.008x + 0.0002 (R^2 = 0.9994) in the linear range of 0.6–300.0 μM, the detection limit (LOD) of the assay was calculated to be 0.18 μM, based on the 3σ/k rule (where σ denotes the standard deviation obtained by conducting blank samples, and k is the slope of the calibration curve) (Figure 5D).[57] Importantly, clear yellow color in this reaction can be directly observed just through naked eyes, which could be applied to sensitive detection of the OP.

To further evaluate the specificity of the assay, various interfering components were introduced, including other organic phosphorus (e.g., parathion, profenofos, isocarbophos, chlorpyrifos and glyphosate) and carbamate esters (e.g., isoprocarb and carbaryl). As shown in Figure 5E, the addition of parathion, profenofos, isocarbophos, chlorpyrifos, glyphosate, isoprocarb and carbaryl did not cause obvious color change. Compared to the responses of other organic phosphorus and carbamate esters, the positive result was only observed with paraoxon (Figure 5E), ascribed to the chromogenic substrate p-NP was only generated by the dephosphorylation reaction of paraoxon, thereby implying its specificity for paraoxon analysis. Simultaneously, as illustrated in Figure 5E, when the analyte was substituted with its analogy parathion, no color changes were observed, suggesting that MOF-808-Apt hardly catalyze the break of –OP=S group of parathions within a brief period. Overall, the above results strongly verified the specificity of the MOF-808-Apt-mediated assay for paraoxon detection. In comparison with the reported methods, the paraoxon sensing platform built in this work is at a leading-edge level in terms of detection limit and detection range, which implies that our system can be applied in a broader range of scenarios (Table S3). Additionally, the recyclability and reusability of MOF-808-Apt were further examined by performing repeated cycles of the hydrolysis reaction, centrifugation, collection and vacuum treatment. MOF-808-Apt showed no significant changes after six cycles under the same conditions (Figure S17). At the same time, the material remained stable after one month of storage (Figure S18). The results indicated the reusability and good stability of MOF-808-Apt, suggesting its considerable potential for practical applications in real-world scenarios.

During the standard addition assay, water samples collected from the Yangtze River and

Taihu Lake (Figure S19 and Table S4) were spiked with paraoxon at concentrations of 5, 50, and 300 μM, respectively, to investigate its application in real aquatic environments. As listed in Table S5, satisfactory recoveries (96.0–103.8%) were obtained, meaning that it is reliable for paraoxon analysis with satisfactory accuracy in environmental waters.

In Situ Monitoring the Hydrolysis of Paraoxon. Owing to its nucleic acid bionic arms, MOF-808-Apt showed unique capability for efficient and selective degradation of OPs, which could be real-time recorded depending on the intensity of bright yellow in reaction solution originated from its degradation product p-NP. Actually, this important property can provide an ideal platform for in situ monitoring the catalytic process of paraoxon hydrolysis, and the dynamic process of hydrolytic cleavage of paraoxon in aqueous solution could be spectrophotometrically measured by monitoring the evolution of p-NP under a wavelength scan from 300 to 500 nm. Shown in Figure 6A, the absorbance spectra of paraoxon upon the addition of MOF-808-Apt were recorded every 2 min within 10 min. Interestingly, due to rapidly increasing of p-NP, the real-time dynamic change of bright yellow can be directly observed just by naked eyes, corresponding to the degree of paraoxon degradation, which is consistent with the gradually increasing absorption measured at 400 nm (Figure 6B).

In summary, our designed biomimetic nanozymes not only could be used as a powerful tool for rapid hydrolysis of typical OPs with excellent selectivity and remarkable efficiency in environmental waters, but also as a sensing system for monitoring this dynamic degradation process in situ simply through color changes, which offered a novel strategy in the study about the degradation mechanism of some pollutants.

ACKNOWLEDGEMENTS

This work was supported by the National Natural Science Foundation of China (Grants No. 22176075 and 22476072), and the Jiangsu Collaborative Innovation Center of Technology and Material of Water Treatment. Besides, ZY also thanks the Leverhulme Trust Research Leadership Awards (RL-2022-041) and the UKRI NERC Fellowship grant (NE/R013349/2).

REFERENCES

(1) Fu, H. Y.; Tan, P.; Wang, R. J.; Li, S. L.; Liu, H. Z.; Yang, Y.; Wu, Z. L., Advances in organophosphorus pesticides pollution: Current status and challenges in ecotoxicological, sustainable agriculture, and degradation strategies. *J. Hazard. Mater.* **2022,** *424*, No. 127494.

(2) Wu, L. P.; Verma, D.; Bondgaard, M.; Melvej, A.; Vogt, C.; Subudhi, S.; Richnow, H. H., Carbon and hydrogen isotope analysis of parathion for characterizing its natural attenuation by hydrolysis at a contaminated site. *Water Res.* **2018,** *143*, 146−154.

(3) Wu, G. X.; Shi, W.; Zheng, L.; Wang, X. Z.; Tan, Z. M.; Xie, E.; Zhang, D. Y., Impacts of organophosphate pesticide types and concentrations on aquatic bacterial communities and carbon cycling. *J. Hazard. Mater.* **2024,** *475*, No. 134824.

(4) Singh, B. K., Organophosphorus-degrading bacteria: ecology and industrial applications. *Nat. Rev. Microbiol.* **2008,** *7* (2), 156−164.

(5) Pundir, C. S.; Malik, A.; Preety, Bio-sensing of organophosphorus pesticides: A review. *Biosens. Bioelectron.* **2019,** *140*, No. 111348.

(6) Sultatos, L. G., Mammalian toxicology of organophosphorus pesticides. *J. Toxicol. Env. Health* **1994,** *43* (3), 271−289.

(7) Chapalamadugu, S.; Chaudhry, G. R., Microbiological and Biotechnological Aspects of Metabolism of Carbamates and Organophosphates. *Crit. Rev. Biotechnol.* **1992,** *12* (5/6), 357–389.

(8) Karaboga, S.; Severac, F.; Collins, E.-M. S.; Stab, A.; Davis, A.; Souchet, M.; Hervé, G., Organophosphate toxicity patterns: A new approach for assessing organophosphate neurotoxicity. *J. Hazard. Mater.* **2024,** *470*, No. 134236.

(9) Liu, T. T.; Zhang, Y. Y.; Shan, Z.; Wu, M. M.; Li, B. C.; Sun, H.; Su, G. Y.; Wang, R.; Zhang, G., Covalent organic framework membrane for efficient removal of emerging trace organic contaminants from water. *Nat. Water* **2023,** *1* (12), 1059−1067.

(10) Hou, M. M.; Shi, Y. L.; Na, G. S.; Zhao, Z. S.; Cai, Y. Q., Increased Human Exposure to Organophosphate Esters via Ingestion of Drinking Water from Water Dispensers: Sources, Influencing Factors, and Exposure Assessment. *Environ. Sci. Tech. Let.* **2021,** *8* (10), 884−889.

(11) Efremenko, E. N.; Sergeeva, V. S., Organophosphate hydrolase - an enzyme catalyzing degradation of phosphorus-containing toxins and pesticides. *Russ. Chem. B+* **2001,** *50* (10), 1826−1832.

(12) Kaushal, J.; Khatri, M.; Arya, S. K., A treatise on Organophosphate pesticide pollution: Current strategies and advancements in their environmental degradation and elimination. *Ecotox. Environ. Safe.* **2021,** *207*, No. 111483.

(13) Chen, T. Y.; Lu, Y. Z.; Xiong, X. R.; Qiu, M. S.; Peng, Y.; Xu, Z. S., Hydrolytic nanozymes: Preparation, properties, and applications. *Adv. Colloid Interface Sci.* **2024,** *323*,

No. 103072.
(14) Zhao, S. M.; Xu, W.; Zhang, W. L.; Wu, H.; Guang, C. E.; Mu, W. M., Overview of a bioremediation tool: organophosphorus hydrolase and its significant application in the food, environmental, and therapy fields. *Appl. Microbiol. Biot.* **2021,** *105* (21−22), 8241−8253.
(15) Gao, L. Z; Zhuang, J.; Nie, L.; Zhang, J. B.; Zhang, Y.; Gu, N.; Wang, T. H.; Feng, J.; Yang, D. L.; Perrett, S.; Yan, X. Y., Intrinsic peroxidase-like activity of ferromagnetic nanoparticles. *Nat. Nanotechnol.* **2007,** *2* (9), 577−583.
(16) Li, S. R.; Zhou, Z. J.; Tie, Z. X.; Wang, B.; Ye, M.; Du, L.; Cui, R.; Liu, W.; Wan, C. H.; Liu, Q. Y.; Zhao, S.; Wang, Q.; Zhang, Y. H.; Zhang, S.; Zhang, H. G.; Du, Y.; Wei, H., Data-informed discovery of hydrolytic nanozymes. *Nat. Commun.* **2022,** *13* (1), 827.
(17) Zhu, N. F.; Liu, C. B.; Liu, R.; Niu, X. H.; Xiong, D. H.; Wang, K.; Yin, D. Q.; Zhang, Z., Biomimic Nanozymes with Tunable Peroxidase-like Activity Based on the Confinement Effect of Metal–Organic Frameworks (MOFs) for Biosensing. *Anal. Chem.* **2022,** *94* (11), 4821−4830.
(18) Koning, M. C. d.; Grol, M. v.; Breijaert, T., Degradation of Paraoxon and the Chemical Warfare Agents VX, Tabun, and Soman by the Metal–Organic Frameworks UiO-66-NH_2, MOF-808, NU-1000, and PCN-777. *Inorg. Chem.* **2017,** *56* (19), 11804−11809.
(19) Qu, L. J.; Zhang, H.; Zhu, J. H.; Yang, G. S.; Aboul-Enein, H. Y., Rapid determination of organophosphorous pesticides in leeks by gas chromatography–triple quadrupole mass spectrometry. *Food Chem.* **2010,** *122* (1), 327−332.
(20) Li, M. H.; Liu, Y. B; Li, F.; Shen, C. S.; Kaneti, Y. V.; Yamauchi, Y.; Yuliarto, B.; Chen, B.; Wang, C. C., Defect-Rich Hierarchical Porous UiO-66(Zr) for Tunable Phosphate Removal. *Environ. Sci. Technol.* **2021,** *55*, 13209−13218.
(21) Kirlikovali, K. O.; Chen, Z. J.; Islamoglu, T.; Hupp, J. T.; Farha, O. K., Zirconium-Based Metal–Organic Frameworks for the Catalytic Hydrolysis of Organophosphorus Nerve Agents. *ACS Appl. Mater. Interfaces* **2020,** *12* (13), 14702−14720.
(22) Ji, P. F.; Feng, X. Y.; Oliveres, P.; Li, Z.; Murakami, A.; Wang, C.; Lin, W. B., Strongly Lewis Acidic Metal–Organic Frameworks for Continuous Flow Catalysis. *J. Am. Chem. Soc.* **2019,** *141* (37), 14878−14888.
(23) Luo, H. B.; Castro, A. J.; Wasson, M. C.; Flores, W.; Farha, O. K.; Liu, Y. Y., Rapid, Biomimetic Degradation of a Nerve Agent Simulant by Incorporating Imidazole Bases into a Metal–Organic Framework. *ACS Catal.* **2021,** *11* (3), 1424−1429.
(24) Ouyang, Y.; Biniuri, Y.; Fadeev, M.; Zhang, P.; Carmieli, R.; Vázquez-González, M.; Willner, I., Aptamer-Modified Cu^{2+}-Functionalized C-Dots: Versatile Means to Improve Nanozyme Activities-"Aptananozymes". *J. Am. Chem. Soc.* **2021,** *143* (30), 11510−11519.
(25) Zhu, F.; Chai, Q. X.; Xiong, D. H.; Zhu, N. F.; Zhou, J. L.; Wu, R. X.; Zhang, Z., Morphology Control of Zr-Based Luminescent Metal-Organic Frameworks for Aflatoxin B1

Detection. *Biosensors* **2024,** *14* (6), 273.
(26) Ouyang, Y.; O'Hagan, M. P.; Willner, B.; Willner, I., Aptamer-Modified Homogeneous Catalysts, Heterogenous Nanoparticle Catalysts, and Photocatalysts: Functional "Nucleoapzymes", "Aptananozymes", and "Photoaptazymes". *Adv. Mater.* **2023,** *36* (10), No. 2210885.
(27) Cheng, P.; Zhu, T. R.; Wang, X. P.; Fan, K. M.; Liu, Y. L.; Wang, X. M.; Xia, S. J., Enhancing Nanofiltration Selectivity of Metal–Organic Framework Membranes via a Confined Interfacial Polymerization Strategy. *Environ. Sci. Technol.* **2023,** *57* (34), 12879−12889.
(28) Ma, K. K; Wasson, M. C.; Wang, X. J.; Zhang, X.; Idrees, K. B.; Chen, Z. J.; Wu, Y. F.; Lee, S. J.; Cao, R.; Chen, Y. W.; Yang, L. F.; Son, F. A.; Islamoglu, T.; Peterson, G. W.; Mahle, J. J.; Farha, O. K., Near-instantaneous catalytic hydrolysis of organophosphorus nerve agents with zirconium-based MOF/hydrogel composites. *Chem Catalysis* **2021,** *1* (3), 721−733.
(29) Ellington, A. D.; Szostak, J. W., In vitro selection of RNA molecules that bind specific ligands. *Nature* **1990,** *346* (6287), 818−822.
(30) Mao, K.; Zhang, H.; Wang, Z. L.; Cao, H. R.; Zhang, K. K.; Li, X. Q.; Yang, Z. G., Nanomaterial-based aptamer sensors for arsenic detection. *Biosens. Bioelectron.* **2020,** *148*, No. 111785.
(31) Michaud, M.; Jourdan, E.; Villet, A.; Ravel, A.; Grosse, C.; Peyrin, E., A DNA Aptamer as a New Target-Specific Chiral Selectorfor HPLC. *J. Am. Chem. Soc.* **2003,** *125*, 8672−8679.
(32) Ma, X. J.; Ou, Q.; Yuan, J. J.; Yang, J. J.; Xu, S. X.; Zhang, X. F., Multifunctional Fe-doped carbon dots and metal-organic frameworks nanoreactor for cascade degradation and detection of organophosphorus pesticides. *Chem. Eng. J.* **2023,** *464*, No. 142480.
(33) Cao, T. W.; Zhang, J. X.; Qi, W.; Wang, M. F., Aptamer-modified Zr-MOFs to construct nanocatalysts with engineered specificity toward paraoxon. *Chem. Commun.* **2023,** *59* (29), 4388−4391.
(34) Xiong, D. H.; Cheng, J.; Ai, F. X.; Wang, X. Y.; Xiao, J. X.; Zhu, F.; Zeng, K.; Wang, K.; Zhang, Z., Insight into the Sensing Behavior of DNA Probes Based on MOF–Nucleic Acid Interaction for Bioanalysis. *Anal. Chem.* **2023,** *95* (12), 5470−5478.
(35) Nguyen, K. D.; Vo, N. T.; Le, K. T. M.; Ho, K. V.; Phan, N. T. S.; Ho, P. H.; Le, H. V., Defect-engineered metal–organic frameworks (MOF-808) towards the improved adsorptive removal of organic dyes and chromium (vi) species from water. *New. J. Chem.* **2023,** *47* (13), 6433−6447.
(36) Ding, J. T.; Guo, D. Y.; Wang, N. S.; Wang, H. F.; Yang, X. F.; Shen, K.; Chen, L. Y.; Li, Y. W., Defect Engineered Metal–Organic Framework with Accelerated Structural Transformation for Efficient Oxygen Evolution Reaction. *Angew. Chem. Int. Ed.* **2023,** *62* (43), No. e202311909.
(37) Jiang, J. C.; Gándara, F.; Zhang, Y. B.; Na, K.; Yaghi, O. M.; Klemperer, W. G.,

Superacidity in Sulfated Metal–Organic Framework-808. *J. Am. Chem. Soc.* **2014,** *136* (37), 12844−12847.

(38) Esken, D.; Turner, S.; Lebedev, O. I.; Van Tendeloo, G.; Fischer, R. A., Au@ZIFs: Stabilization and Encapsulation of Cavity-Size Matching Gold Clusters inside Functionalized Zeolite Imidazolate Frameworks, ZIFs. *Chem. Mater.* **2010,** *22* (23), 6393−6401.

(39) Lu, J. Y.; Wang, M. H.; Han, Y. W.; Deng, Y.; Zeng, Y. J.; Li, C.; Yang, J.; Li, G. X., Functionalization of Covalent Organic Frameworks with DNA via Covalent Modification and the Application to Exosomes Detection. *Anal. Chem.* **2022,** *94* (12), 5055−5061.

(40) Xu, M.; Feng, L.; Yan, L. N.; Meng, S. S.; Yuan, S.; He, M. J.; Liang, H.; Chen, X. Y.; Wei, H. Y.; Gu, Z. Y.; Zhou, H. C., Discovery of precise pH-controlled biomimetic catalysts: defective zirconium metal–organic frameworks as alkaline phosphatase mimics. *Nanoscale* **2019,** *11* (23), 11270−11278.

(41) Momeni, M. R.; Cramer, C. J., Computational Screening of Roles of Defects and Metal Substitution on Reactivity of Different Single- vs Double-Node Metal–Organic Frameworks for Sarin Decomposition. *J. Phys. Chem. C* **2019,** *123* (24), 15157−15165.

(42) Garibay, S. J.; Tovar, T. M.; Iordanov, I. O.; Peterson, G. W.; DeCoste, J. B., Enhancement of catalytic hydrolysis activity for organophosphates by the metal–organic framework MOF-808-NH_2 via post-synthetic modification. *J. Mater. Chem. A* **2023,** *11* (25), 13300−13308.

(43) Zhang, W. T.; Huang, W. G.; Jin, J. Y.; Gan, Y. H.; Zhang, S. J., Oxygen-vacancy-mediated energy transfer for singlet oxygen generation by diketone-anchored MIL-125. *Appl. Catal. B-Environ.* **2021,** *292*, No. 120197.

(44) Sun, C. Y.; Ji, Y. H.; Bi, K. C.; Tian, H. P.; Wang, C. D.; Deng, F. L.; Zhang, Y., Tuning oxygen vacancy and missing linkers of defective MOF-808 for advanced adsorption of Yb(III) from aqueous solution. *Sep. Purif. Technol.* **2024,** *347*, No. 127585.

(45) Ye, G.; Wan, L. L.; Zhang, Q. L.; Liu, H.; Zhou, J.; Wu, L.; Zeng, X. Y.; Wang, H. L.; Chen, X. X.; Wang, J., Boosting Catalytic Performance of MOF-808(Zr) by Direct Generation of Rich Defective Zr Nodes via a Solvent-Free Approach. *Inorg. Chem.* **2023,** *62* (10), 4248-4259.

(46) Fan, M. Y.; Zhang, P.; Wang, C. P.; Tang, J. C.; Sun, H. W., Tailored design of three-dimensional rGOA-nZVI catalyst as an activator of persulfate for degradation of organophosphorus pesticides. *J. Hazard. Mater.* **2022,** *428*, No. 128254.

(47) Xu, L. H.; Li, S. H.; Mao, H.; Li, Y.; Zhang, A. S.; Wang, S.; Liu, W. M.; Lv, J.; Wang, T.; Cai, W. W.; Sang, L.; Xie, W. W.; Pei, C.; Li, Z. Z.; Feng, Y. N.; Zhao, Z. P., Highly flexible and superhydrophobic MOF nanosheet membrane for ultrafast alcohol-water separation. Science **2022**, *378* (6617), 308–313.

(48) Hui, X. B.; Zhan, Z.; Zhang, Z. Y.; Yu, J. Y.; Jiang, P. Y.; Dang, Z. Z.; Wang, J.; Cai, S. H.; Wang, Y. M.; Xu, Z. L., Missing-Linker Defect Functionalized Metal–Organic Frameworks

Accelerating Zinc Ion Conduction for Ultrastable All-Solid-State Zinc Metal Batteries. ACS Nano **2024**, *18* (36), 25237–25248.

(49) Wei, J. C.; Yang, L. L.; Luo, M.; Wang, Y. T.; Li, P., Nanozyme-assisted technique for dual mode detection of organophosphorus pesticide. *Ecotox. Environ. Safe.* **2019,** *179*, 17−23.

(50) Li, T.; Zhong, W.; Jing, C. Y.; Li, X. G.; Zhang, T.; Jiang, C. J.; Chen, W., Enhanced Hydrolysis of p-Nitrophenyl Phosphate by Iron (Hydr)oxide Nanoparticles: Roles of Exposed Facets. *Environ. Sci. Technol.* **2020,** *54* (14), 8658−8667.

(51) Wang, L.; Liu, X. J.; Zhang, Q.; Zhang, C. Z.; Liu, Y.; Tu, K.; Tu, J., Selection of DNA aptamers that bind to four organophosphorus pesticides. *Biotechnol. Lett.* **2012,** *34* (5), 869−874.

(52) Alkhamis, O.; Canoura, J.; Wu, Y.; Emmons, N. A.; Wang, Y.; Honeywell, K. M.; Plaxco, K. W.; Kippin, T. E.; Xiao, Y., High-Affinity Aptamers for In Vitro and In Vivo Cocaine Sensing. *J. Am. Chem. Soc.* **2024,** *146* (5), 3230−3240.

(53) Dou, X. L.; Wu, G.; Ding, Z. Y.; Xie, J., Construction of a nanoscale metal-organic framework aptasensor for fluorescence ratiometric sensing of AFB1 in real samples. *Food Chem.* **2023,** *416*, No. 135805.

(54) Hardian, R.; Dissegna, S.; Ullrich, A.; Llewellyn, P. L.; Coulet, M. V.; Fischer, R. A., Tuning the Properties of MOF-808 via Defect Engineering and Metal Nanoparticle Encapsulation. *Chem-Eur. J.* **2021,** *27* (22), 6804−6814.

(55) Lv, M. Z.; Zhou, W.; Tavakoli, H.; Bautista, C.; Xia, J. F.; Wang, Z. H.; Li, X. J., Aptamer-functionalized metal-organic frameworks (MOFs) for biosensing. *Biosens. Bioelectron.* **2021,** *176*, No. 112947.

(56) Li, Y. C.; Wang, P.; Huang, L. J.; Jia, C. H.; Gao, X.; Liu, S. J.; Wang, S. C.; Zhao, P.; Sun, J.; Zhang, D. H.; Zhu, M. Q.; Shen, Y. Z.; Wang, J. L., Schiff-Base Chemistry-Coupled Catechol Oxidase-Like Nanozyme Reaction as a Universal Sensing Mode for Ultrasensitive Biosensing. *Anal. Chem.* **2023,** *95* (7), 3769−3778.

(57) Kang, Y. L.; Su, G. X.; Yu, Y. Y.; Cao, J. J.; Wang, J. L.; Yan, B., CRISPR-Cas12a-Based Aptasensor for On-Site and Highly Sensitive Detection of Microcystin-LR in Freshwater. *Environ. Sci. Technol.* **2022,** *56* (7), 4101−4110.

Figure

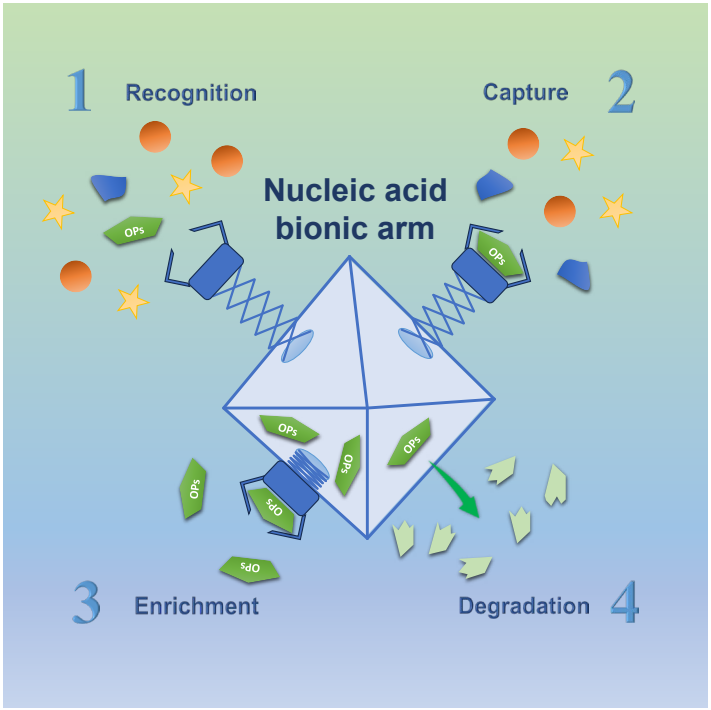

Scheme 1. Schematic diagram of targeted enrichment of organophosphorus pesticides by nucleic acid bionic arms modified on Zr–MOFs.

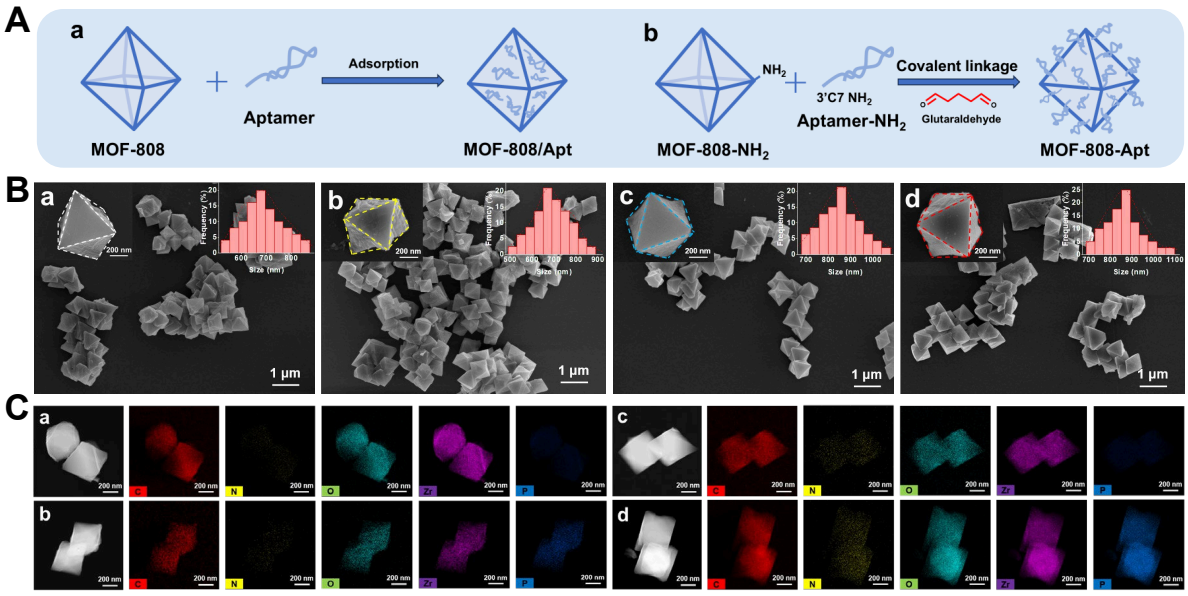

Figure 1. (A) Schematic illustrations of the synthetic process of (a) MOF-808/Apt and (b) MOF-808-Apt. (B) SEM images of (a) MOF-808, (b) MOF-808/Apt, (c) MOF-808-NH_2 and (d) MOF-808-Apt. (C) HAADF images and elemental mappings of (a) MOF-808, (b) MOF-808/Apt, (c) MOF-808-NH_2 and (d) MOF-808-Apt.

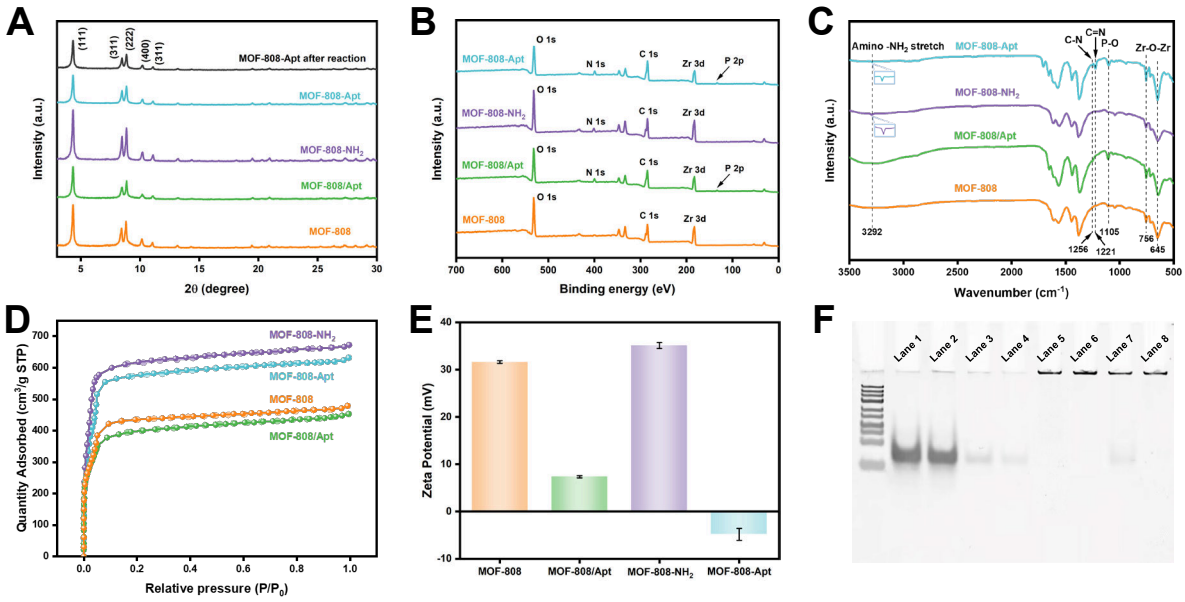

Figure 2. (A) XRD patterns of MOF-808, MOF-808/Apt, MOF-808-NH_2, MOF-808-Apt and MOF-808-Apt after reaction. (B) XPS spectra, (C) FT-IR spectra, (D) Nitrogen physisorption isotherm, (E) Zeta potential of MOF-808, MOF-808/Apt, MOF-808-NH_2 and MOF-808-Apt. (F) Polyacrylamide gel analysis. Lane 1: Aptamer; lane 2: Aptamer+paraoxon; lane 3: Supernatant of MOF-808/Apt; lane 4: Supernatant of MOF-808-Apt; lane 5: MOF-808/Apt; lane 6: MOF-808-Apt; lane 7: MOF-808/Apt after reaction; lane 8: MOF-808-Apt after reaction.

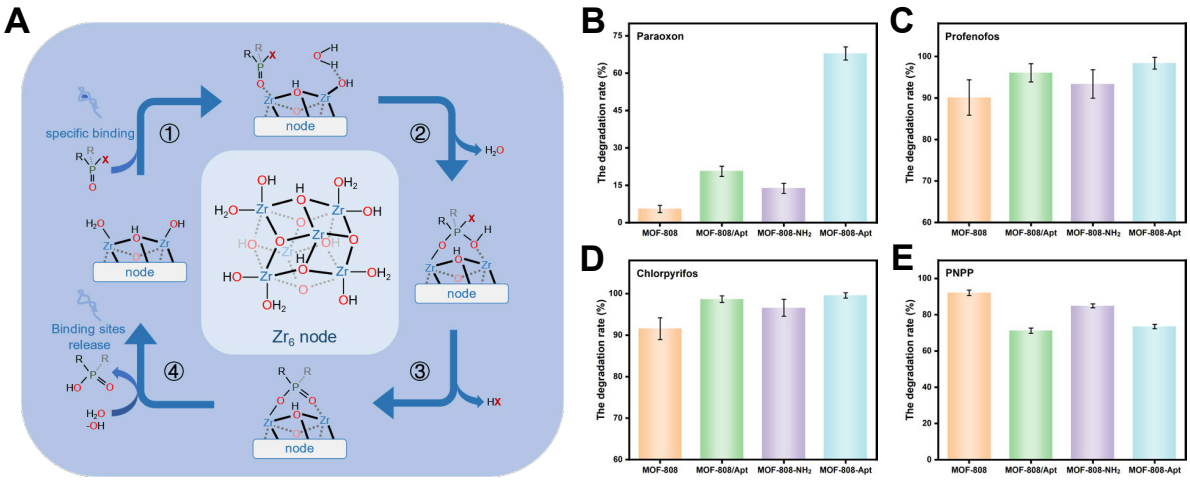

Figure 3. (A) Catalytic cycle of Zr–MOFs-based organophosphorus hydrolysis catalysts modified by aptamers. Comparison of degradation rates of (B) paraoxon, (C) profenofos, (D) chlorpyrifos and (E) PNPP by MOF-808, MOF-808/Apt, MOF-808-NH_2 and MOF-808-Apt.

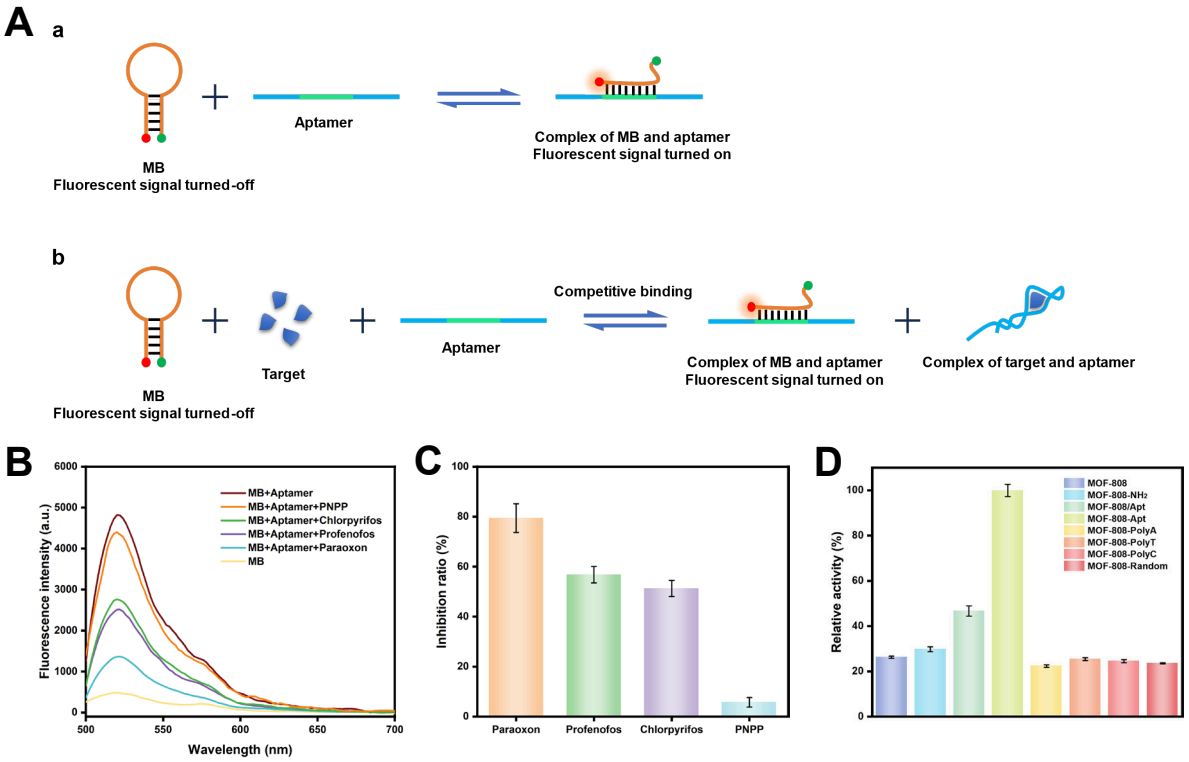

Figure 4. (A) Strategy for the determination of different affinities of the aptamers against OPs: the green area in the aptamer presents the constant sequences, which can complementary binding to MB. (a) present the control model with chemical absence and (b) present the competition model with chemical presence; compared with the condition (a), the turn-on fluorescent signal in condition (b) will be decreased by the chemical competitively binding to aptamer, and the changes in fluorescence is associated with the changes in the concentration of the chemical. (B) Fluorescence response of MB and aptamers without and with paraoxon, profenofos, chlorpyrifos and PNPP. (C) Inhibition ratio of fluorescence response after adding paraoxon, profenofos, chlorpyrifos and PNPP. (D) Comparison of the catalytic activities of the poly(A), poly(C), poly(T), random DNA chains and aptamers modified MOF-808.

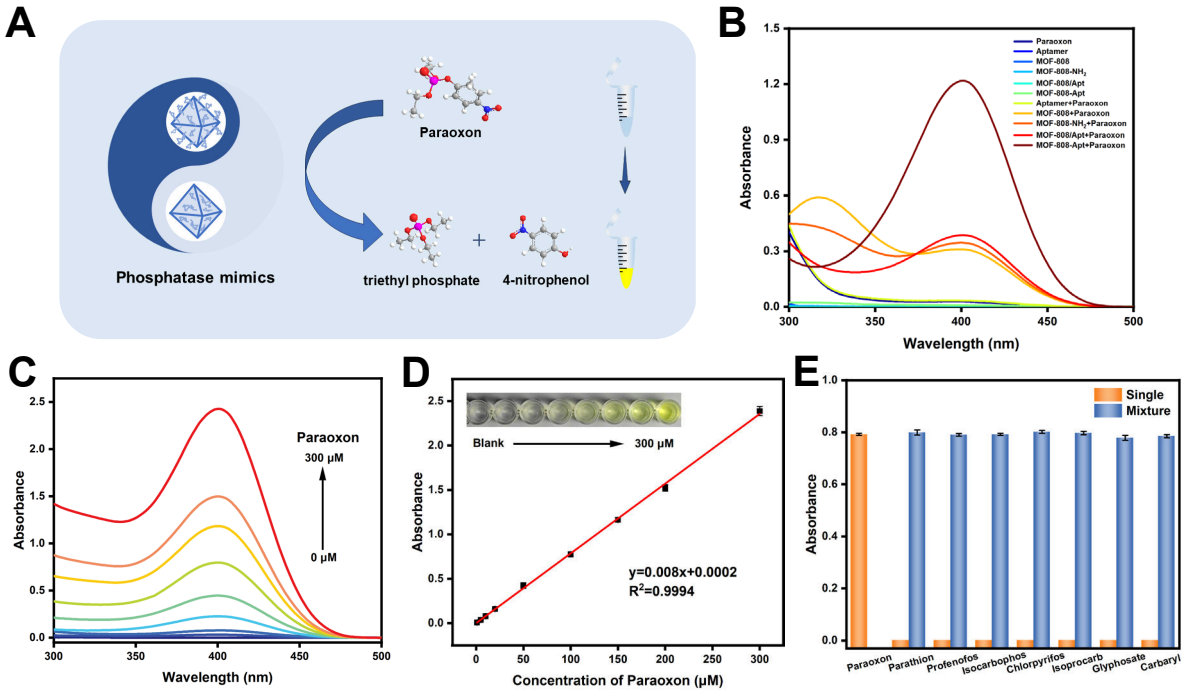

Figure 5. (A) Schematic diagram of colorimetric analysis method for paraoxon. (B) Comparison of the absorbance at 400nm after the hydrolysis reaction of different materials with paraoxon. (C) Absorption spectra of the analytical platform respond to varying concentrations of paraoxon from 0 to 300 μM. (D) Working curve for paraoxon detection (Insets: photograph of the assay system containing various concentration of paraoxon). (E) Selectivity and anti-interference experiment using MOF-808-Apt for detection of paraoxon. Experimental conditions: MOF-808-Apt, 0.3 mg/mL; paraoxon and other OPs 100 μM; 1.5 mM pH 9.0 NEM buffer.

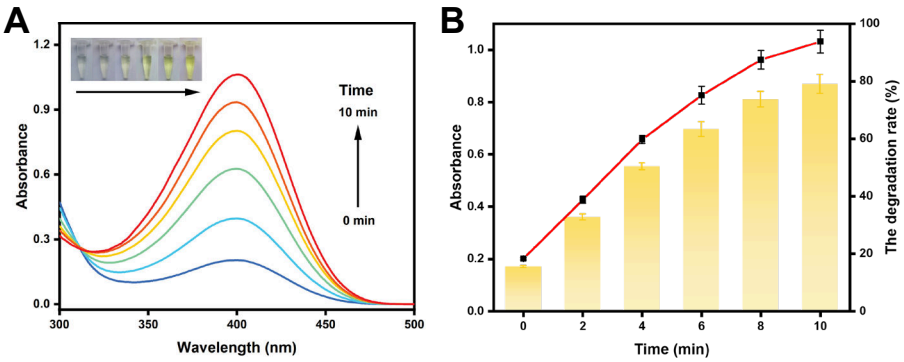

Figure 6. (A) Time-dependent absorption spectra changes of the MOF-808-Apt in paraoxon solution. The spectra were recorded at intervals of 10 min. The inset is the photographs of paraoxon solution in the presence of MOF-808-Apt in natural light. (B) Plots of versus time for the catalytic hydrolytic cleavage of paraoxon at room temperature.

Supporting Information

Targeted Enrichment of Nucleic Acid Bionic Arms Enhance Hydrolysis Activity of Nanozymes for Degradation and Real-time Monitoring of Organophosphorus Pesticides in Water

Jialong Zhou,[1] Dinghui Xiong,[1] Hu Zhang,[1] Jiaxuan Xiao,[1] Rui Huang,[1,2] Ze Qiao,[1,2] Zhugen Yang[2]* and Zhen Zhang[1]*

[1]School of the Environment and Safety Engineering, Jiangsu University, Zhenjiang, 212013, China

[2]Faculty of Engineering and Applied Sciences, Cranfield University, Milton Keynes, MK43 0AL, UK

*Corresponding author:

E-mail: zhugen.yang@cranfield.ac.uk, zhangzhen@ujs.edu.cn

Fax: +86-511-88790955

Supporting information including 10 Text, 21 Figures, and 5 Tables.

Text S1. Reagents

All aptamers were synthesized and purified by Sangon Biotechnology Company, Ltd. (Shanghai, China), and the sequences are illustrated in **Table S1**. Paraoxon, parathion, profenofos, isocarbophos, chlorpyrifos, glyphosate, isoprocarb and carbaryl were all purchased from Beijing Tan Mo Quality Inspection Technology Co., Ltd. Zirconyl chloride octahydrate ($ZrOCl_2 \cdot 8H_2O$), 1,3,5-Benzenetricarboxylic acid (H_3BTC) and 5-aminoisophthalic acid ($H_2BTC\text{-}NH_2$) were purchased from Bide Pharmsatech Co., Ltd (Shanghai, China). p-nitrophenyl phosphate disodium salt (PNPP), N, N-dimethylformamide (DMF), formic acid, acetone, acetonitrile, methanol, Glutaraldehyde (25 wt% aqueous water), 4-hydroxyethyl piperazine ethyl sulfonic acid (HEPES), and N-Ethylmorpholine were purchased from Aladdin Biochemical Technology Co., Ltd (Shanghai, China). All the reagents used in this work were of analytical grade without further purification, and water was ultrapure water.

Text S2. Instruments

The field emission scanning electron microscopy (FESEM) imaging was done with a FESEM instrument (JSM-7800F, JEOL, Japan); The transmission electron microscope (TEM) imaging, color mapping and energy dispersive spectroscopy (EDS) analyses were performed using the JEM-2100 TEM instrument (JEOL, Japan) with a separate EDS detector (JEM-2100 F, JEOL, Japan) connected to that instrument; X-ray diffraction (XRD) patterns were obtained from a diffractometer (D8 ADVANCE, Bruker, Germany); X-ray photoelectron spectroscopy (XPS) was recorded by AXIS SUPRA. Fourier transform infrared (FTIR) measurements were carried out with a Nexus 460 FTIR spectrometer (Thermo Nicolet, USA); The particle size and zeta potential were determined using the zetasizer analyzer (Nano ZS90, Malvern, UK); 7000, Japan). The Bruneian-Emmett-Teller (BET) surface area was obtained by nitrogen adsorption/desorption measurement instrument (JW-BK200B, China). The water contact angle was measured by optical contact angle and interface tension meter (KINO SL 200 KB, USA). The electron paramagnetic resonance (EPR) signals were obtained by A300 spectrometer (Bruker, Germany). The Raman spectra were collected with the Laser Raman spectroprobe (LM2000, Renishaw, UK). The liquid chromatography/mass spectrometry (LC/MS) (Agilent Revident LC/Q-TOF, USA.) equipped with a variable wavelength UV detector (G1314B/C) was employed to detect degradation products based on Agilent Poroshell 120 EC-C18 (100

mmx2.1 mm, 2.7 um) chromatographic column. Ultraviolet photoemission spectroscopy (UPS) characterization was carried out by a VG Scienta R3000 analyzer in ultrahigh vacuum; The UV-Vis absorption spectra were obtained using the UV-Vis spectrophotometer (UV-2600, SHIMADZU, Japan). Additionally, the fluorescence spectra and absorption spectra were recorded with a microplate reader (Infinite M1000 Pro, TECAN, Switzerland).

Text S3. Preparation of MOF-808 and MOF-808-NH_2

$ZrOCl_2 \cdot 8H_2O$ (0.54 g, 1.67 mmol) and H_3BTC (0.12 g, 0.57 mmol) were dissolved separately using 50 mL of a mixture of DMF and formic acid (1:1, v/v) in total. The mixture was sealed and heated to 80°C in an oven for 72 h. After cooling to room temperature, the solid was collected and washed with DMF (3×20 mL) and acetone (3×20 mL). The solid product was then dried under vacuum at 120°C for 5 h to obtain MOF-808.

$ZrOCl_2 \cdot 8H_2O$ (0.54 g, 1.67 mmol), H_3BTC (0.09 g, 0.43 mmol) and H_2BTC-NH_2 (0.026 g, 0.143 mmol) were dissolved separately using 50 mL of a mixture of DMF and formic acid (1:1, v/v) in total. The mixture was sealed and heated to 80°C in an oven for 72 h. After cooling to room temperature, the solid was collected and washed with DMF (3×20 mL) and acetone (3×20 mL). The solid product was then dried under vacuum at 120°C for 5 h to obtain MOF-808-NH_2.

Text S4. Preparation of MOF-808/Apt and MOF-808-Apt

MOF-808 was dispersed in 500 μL of ultrapure water to the concentration of 5 mg/mL. Then, aptamers were added to the suspension of MOF-808. The reaction continued at 4°C for 1 h, and the suspension was centrifuged, washed and re-dispersed with ultrapure water (containing 50 mM NaCl, 10mM KCl and 10 mM $MgCl_2$) to obtain MOF-808/Apt, and finally stored at 4°C for future use.

Additionally, MOF-808-NH_2 was dispersed in 500 μL of ultrapure water to the concentration of 5 mg/mL. Then, 500 μL of glutaraldehyde (2.5 wt% in aqueous water) was added, and the reaction was carried out at room temperature for 2 h on a rotary oscillator at a speed of 50 r/min. Then, the supernatant was removed by centrifugation, and 400 μL of HEPES buffer (20 mM, pH 7.4) and 100 μL of aptamers were added. The reaction continued at 37°C for 24 h, and the suspension was centrifuged, washed and re-dispersed with ultrapure water (containing 50 mM NaCl, 10mM KCl and 10 mM $MgCl_2$) to obtain MOF-808-Apt, and finally stored at 4°C

for future use.

Text S5. Degradation of Organophosphorus Compounds by Biomimetic Nanozymes

In a typical process, 100 μM different freshly prepared organophosphorus compounds (paraoxon, profenofos, isocarbophos and PNPP) were introduced into 0.3 mg/mL biomimetic nanozymes (MOF-808, MOF-808/Apt, MOF-808-NH_2 and MOF-808-Apt) in NEM buffer (1.5 mM, pH 9.0, containing 50 mM NaCl, 10 mM KCl and 10 mM $MgCl_2$), respectively. The residual paraoxon, profenofos, isocarbophos and PNPP in the filtrate obtained by centrifugation was determined by HPLC-MS after the reaction. The measurement by HPLC-MS was performed by Chongyan Technology Co., Ltd. (Suzhou, China)

Conditions for detecting paraoxon: methanol/water mixture (V/V, 85/15) as a mobile phase, and flow rate, detection wavelength, column temperature and injection volume were fixed to be 0.5 mL/min, 274 nm, 25°C and 20.0 μL, respectively. The ion source of mass spectrometry was set to ESI+ and Ion source temperature was set to 500°C.

Conditions for detecting profenofos: 0.1% formic acid/acetonitrile mixture (V/V, 90/10) as a mobile phase, and flow rate, detection wavelength, column temperature and injection volume were fixed to be 0.2 mL/min, 274 nm, 40°C and 5.0 μL, respectively. The ion source of mass spectrometry was set to ESI+ and Ion source temperature was set to 300°C.

Conditions for detecting chlorpyrifos: methanol/water mixture (V/V, 90/10) as a mobile phase, and flow rate, detection wavelength, column temperature and injection volume were fixed to be 0.25 mL/min, 274 nm, 40°C and 3.0 μL, respectively. The ion source of mass spectrometry was set to ESI+ and Ion source temperature was set to 500°C.

Conditions for detecting PNPP: methanol/ammonium formate - formic acid aqueous solution mixture (V/V, 75/25) as a mobile phase, and flow rate, detection wavelength, column temperature and injection volume were fixed to be 0.2 mL/min, 274 nm, 30°C and 10.0 μL, respectively. The ion source of mass spectrometry was set to ESI+ and Ion source temperature was set to 500°C.

Matrixmatched external standard calibration was used for quantitative analysis in this work. In detail, standard samples of organophosphorus compounds (paraoxon, profenofos, isocarbophos and PNPP) with certain concentration swere prepared using the same matrix as the unknown samples to ensure that any matrix-related interference is accounted for in the

calibration process. Subsequently, the chromatographic and mass spectra of the samples after degradation were recorded and the corresponding peak areas were analyzed to calculate the concentration of the analyte. And the degradation rate was calculated by the equation, i.e., $(1-C/C_0) \times 100\%$, where C_0 and C were the concentration of before and after the degradation of organophosphorus compounds, respectively.

Text S6. Aptamer Binding Competitive Assay

The strategy for competitive assay development was to incubate the aptamer with the chemical for 11 min first, and then the molecular beacon (MB) was added to turn on the signal for detection, and the homogeneous assay was performed at 37°C for 50 min in NEM buffer (1.5 mM, pH 9.0, containing 50 mM NaCl, 10 mM KCl and 10 mM $MgCl_2$) with a final acetone content of below 1%. Fluorescence intensities were recorded and the excitation and emission wavelengths were set at 485 and 535 nm, respectively. All spectra were obtained at 37 ºC in buffer solution. The inhibition ratio was calculated using the following equation:

$$IR\ (\%) = (C-T)/(C-B) \times 100\%$$

Where T and C are the observed fluorescence intensities of DNA aptamers binding MB duplexes in the presence and absence of chemicals, respectively; B is the background fluorescence intensity; and IR represents the ratio of inhibition connecting the fluorescence intensities and concentrations of chemicals.

Text S7. Catalytic Kinetics Assay of Biomimetic Nanozymes

Kinetic measurements of phosphatase-like property were confirmed by the color change of p-nitrophenol (p-NP), which is indicated by the absorbance at 400 nm recorded by a multimode reader. The kinetic data were recorded with the change of paraoxon concentration. As for the kinetic data toward paraoxon, 50 μL of biomimetic nanozymes (0.3 mg/mL) were added into the mixture, including 400 μL of NEM buffer (1.5 mM, pH 9.0, containing 50 mM NaCl, 10 mM KCl and 10 mM $MgCl_2$), and 50 μL of different concentrations of paraoxon (20, 30, 50, 80, 100, 200 μM). The kinetic data were calculated by a typical Michaelis-Menten curve as to $v = V_{max}[S] / (K_m + [S])$, where v is the initial velocity, [S] is the concentration of the substrate, K_m is the Michaelis-Menten constant, and V_{max} is the maximal reaction velocity.

Text S8. Colorimetric Biosensing of Paraoxon

50 μL various concentrations of paraoxon (0, 5, 10, 20, 50, 100, 150, 200, 300 μM) and 400 μL NEM buffer (1.5 mM, pH 9.0, containing 50 mM NaCl, 10 mM KCl and 10 mM $MgCl_2$) were added into the centrifuged tube in the presence of 50 μL MOF-808-Apt (0.3 mg/mL). After incubation at 37°C for 6 min, the reactants were centrifuged at 11000 r/min for 3 minutes. 200 μL of the supernatants was transferred into cuvette, and the UV-Vis signal was monitored in the wavelength range of 300-500 nm. The absorbance was recorded at wavelength of 400 nm.

Text S9. Determination of Paraoxon in Real Water Samples

To test the practicability of our developed biosensor, Yangtze River water sample and Taihu Lake water sample that had been certified as free of paraoxon were used for the recovery studies.

The water samples with different sources were respectively collected from Yangtze River (32°11'10"N, 119°17'30"E) and Taihu Lake (31°28'50"N, 120°02'40"E), both located in Yangtze River Delta (**Figure S19**). Additionally, the water quality monitoring data of sampling sites were provided in **Table S4**, which is obtained from the local government.

After simple preprocessor various concentrations of paraoxon (5, 50, 300 μM) were spiked in these real water samples and analyzed.

Text S10. In Situ Monitoring the Hydrolysis of Paraoxon

50 μL paraoxon (100 μM), 50 μL MOF-808-Apt solution (0.3 mg/mL) and 400 μL NEM buffer solution (1.5 mM, pH 9.0, containing 50 mM NaCl; KCl 10 mM and $MgCl_2$ 10 mM), reacts at 37°C, and with the reaction time from 0 min to 10 min, the yellow change was observed by naked eye in real time or the absorbance value at 400 nm wavelength was analyzed in real time by ultraviolet spectrophotometer to monitor the degree of paraoxon degradation.

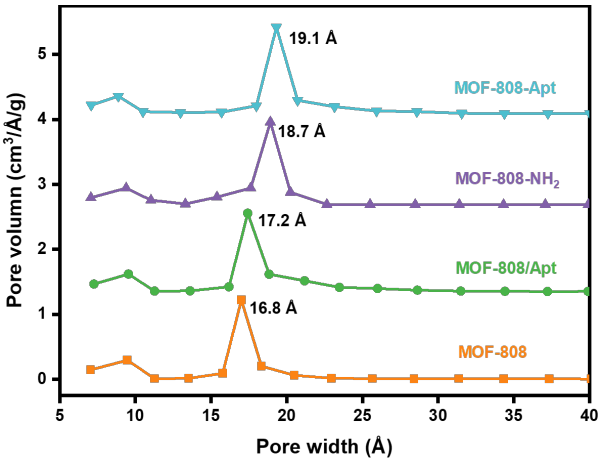

Figure S1. The pore size distribution of MOF-808, MOF-808/Apt, MOF-808-NH_2 and MOF-808-Apt.

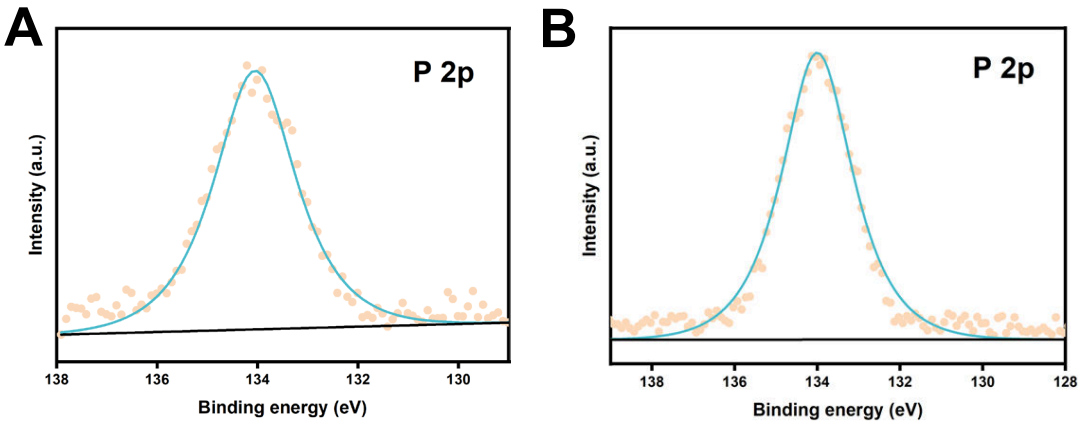

Figure S2. The high-resolution XPS spectrum of additional P 2p signal of (A) MOF-808/Apt and (B) MOF-808-Apt.

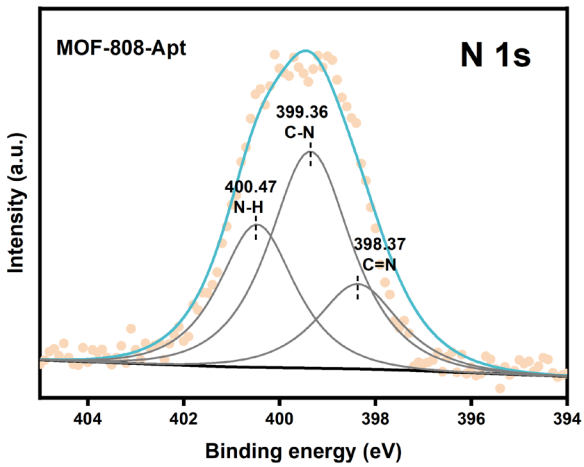

Figure S3. The high-resolution XPS spectrum of N 1s signal of MOF-808-Apt.

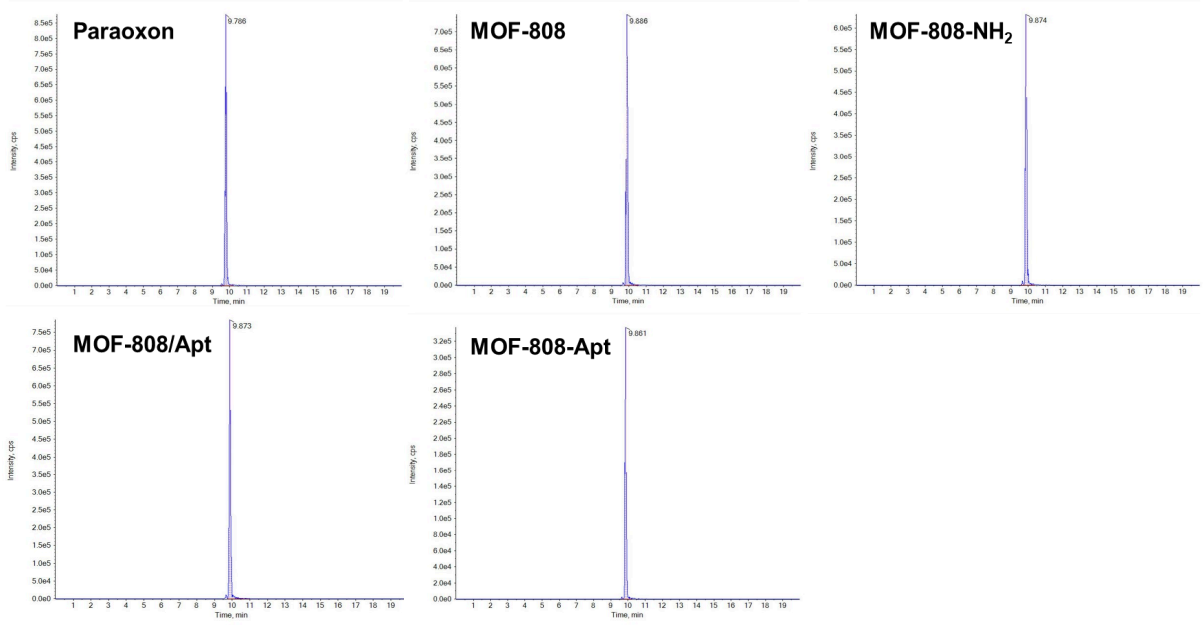

Figure S4. The HPLC-MS of (A) paraoxon and paraoxon degraded by (B) MOF-808, (C) MOF-808/Apt, (D) MOF-808-NH_2 and (E) MOF-808-Apt.

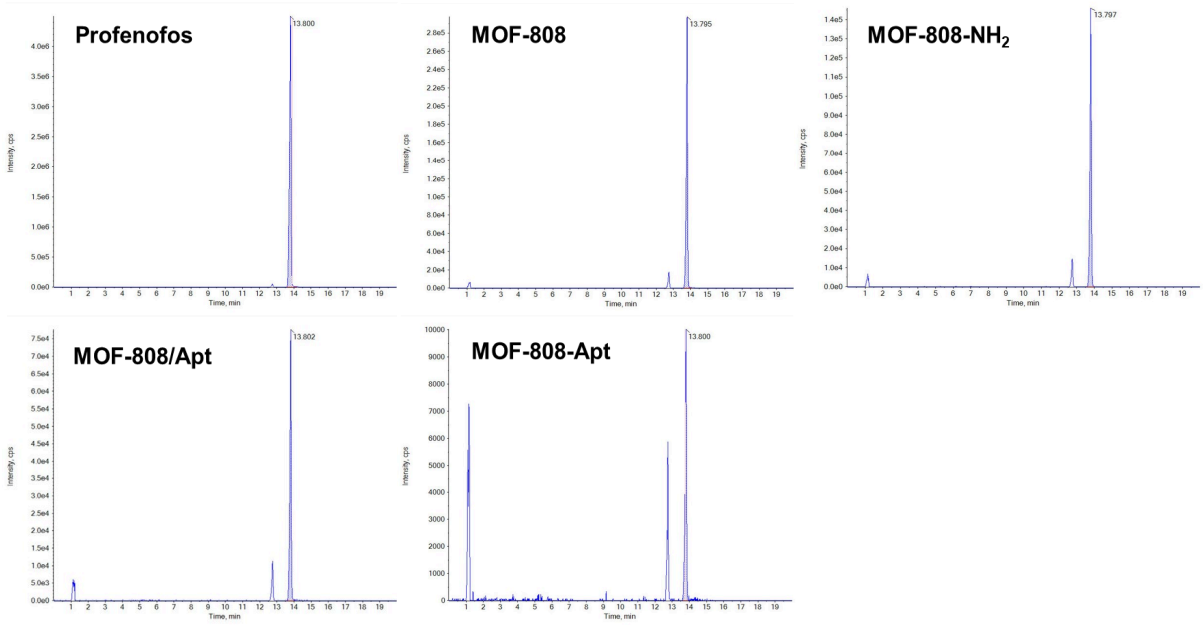

Figure S5. The HPLC-MS of (A) profenofos and profenofos degraded by (B) MOF-808, (C) MOF-808/Apt, (D) MOF-808-NH_2 and (E) MOF-808-Apt.

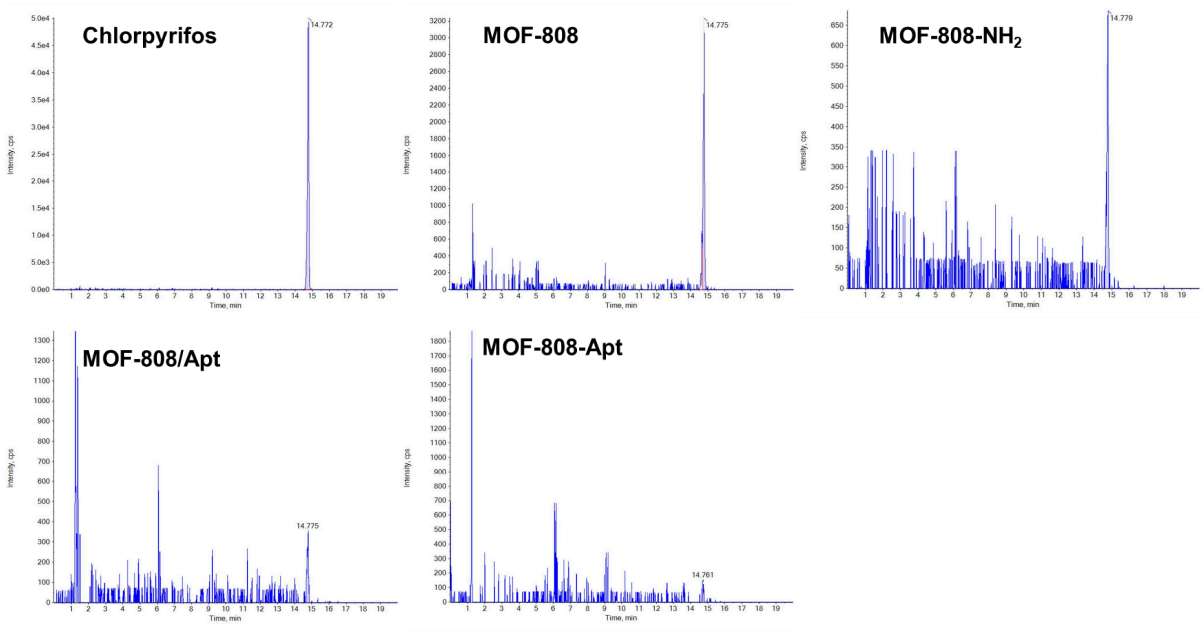

Figure S6. The HPLC-MS of (A) Chlorpyrifos and Chlorpyrifos degraded by (B) MOF-808, (C) MOF-808/Apt, (D) MOF-808-NH_2 and (E) MOF-808-Apt.

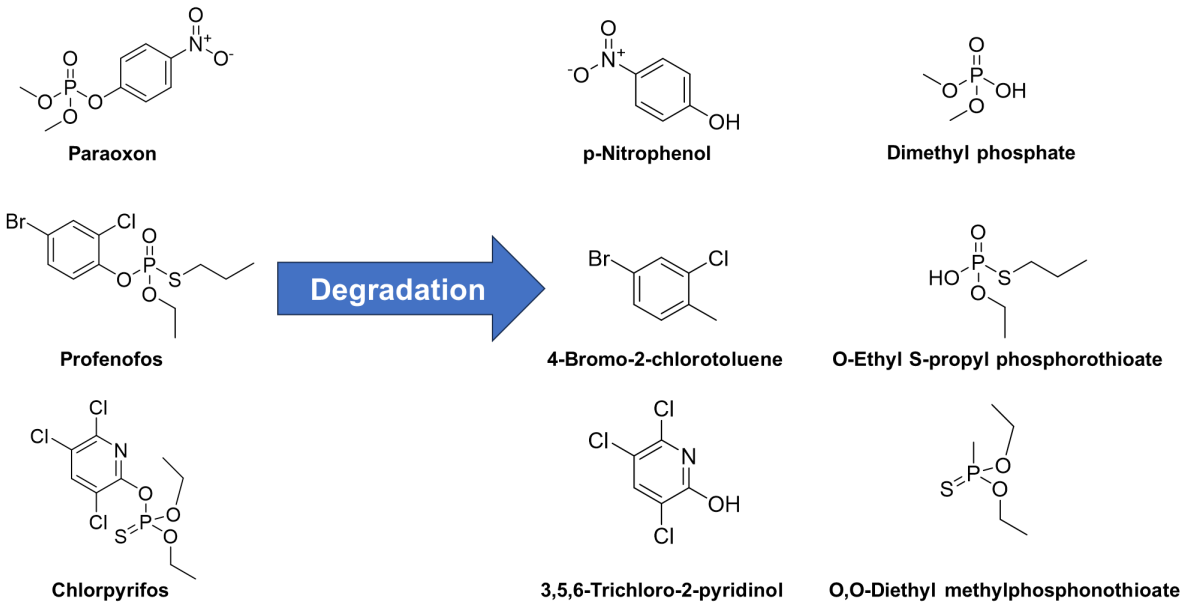

Figure S7. The structural formula of typical OPs and their degradation products.

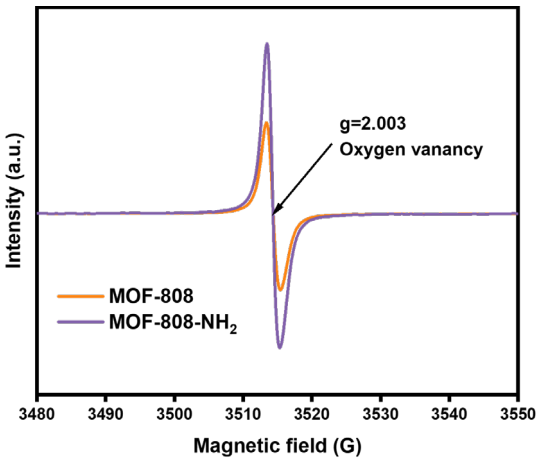

Figure S8. EPR spectra of MOF-808 and MOF-808-NH_2.

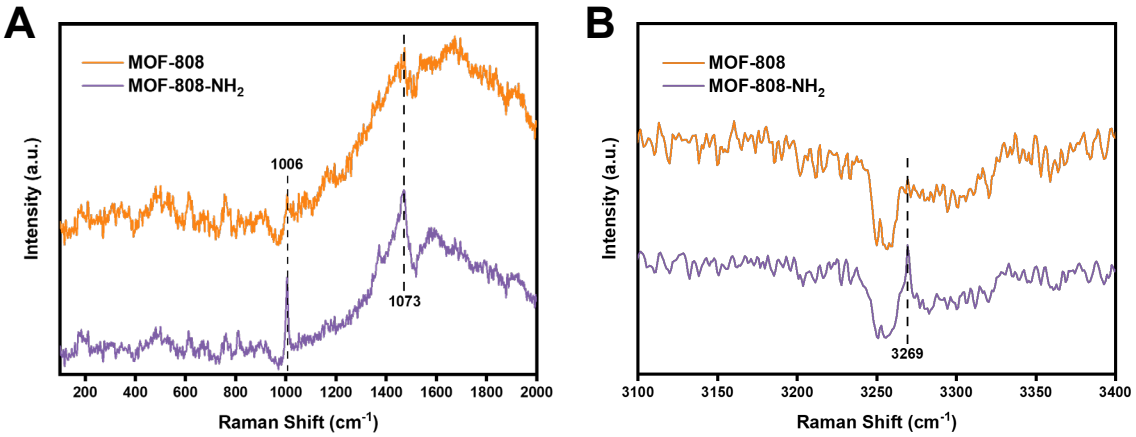

Figure S9. Raman spectra of MOF-808 and MOF-808-NH_2.

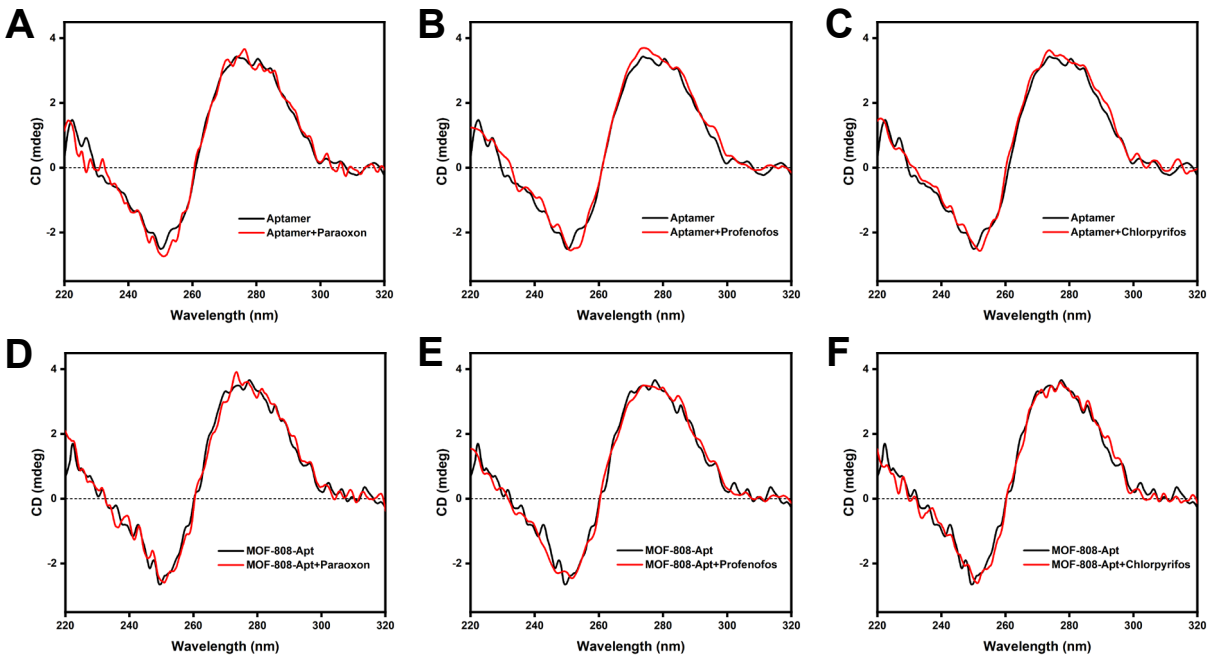

Figure S10. CD of aptamer without and with (A) Paraoxon, (B) Profenofos and (C) Chlorpyrifos. CD of aptamer on MOF-808 without and with (D) Paraoxon, (E) Profenofos and (F) Chlorpyrifos.

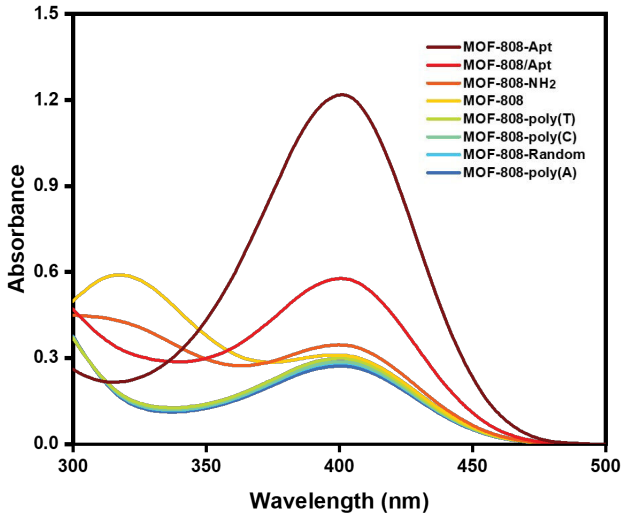

Figure S11. Comparison of the absorbance at 400nm after the hydrolysis reaction with paraoxon of the poly(A), poly(C), poly(T), random DNA chains and aptamers modified MOF-808.

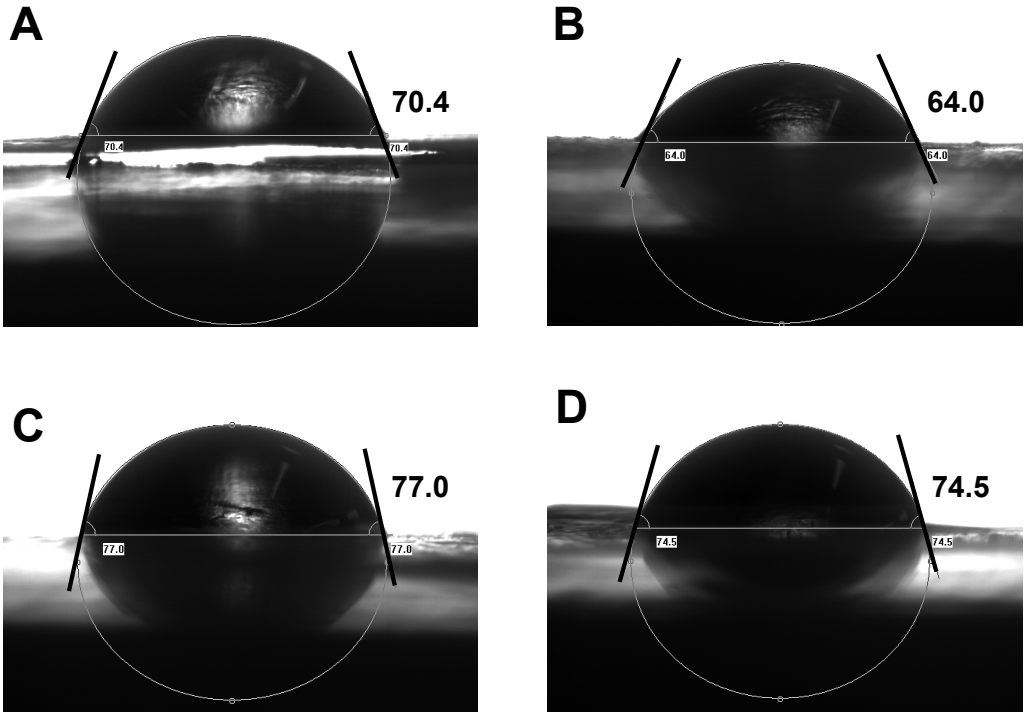

Figure S12. Results for the water contact angle measurement, (a) MOF-808, (B) MOF-808-NH_2, (C) MOF-808/Apt and (D) MOF-808-Apt.

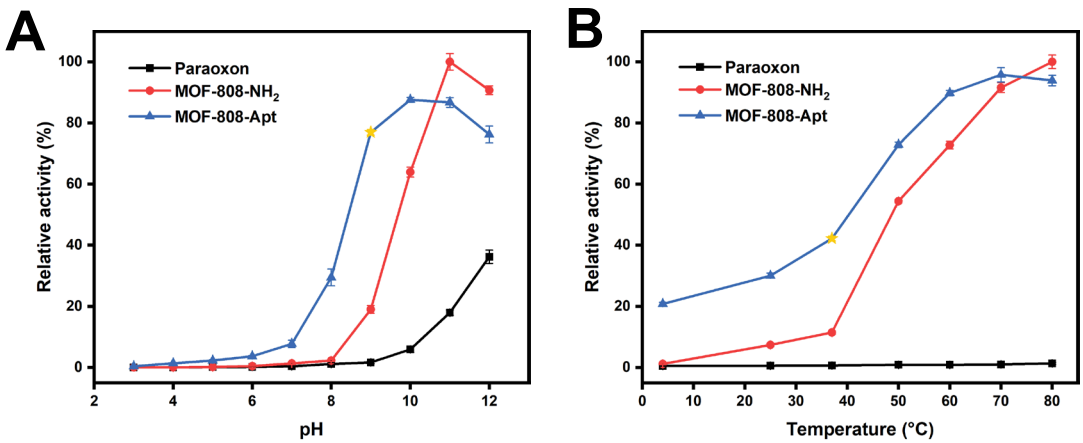

Figure S13. The catalytic ability of MOF-808-NH_2 and MOF-808-Apt on Paraoxon under different (A) pH and (B) temperature conditions.

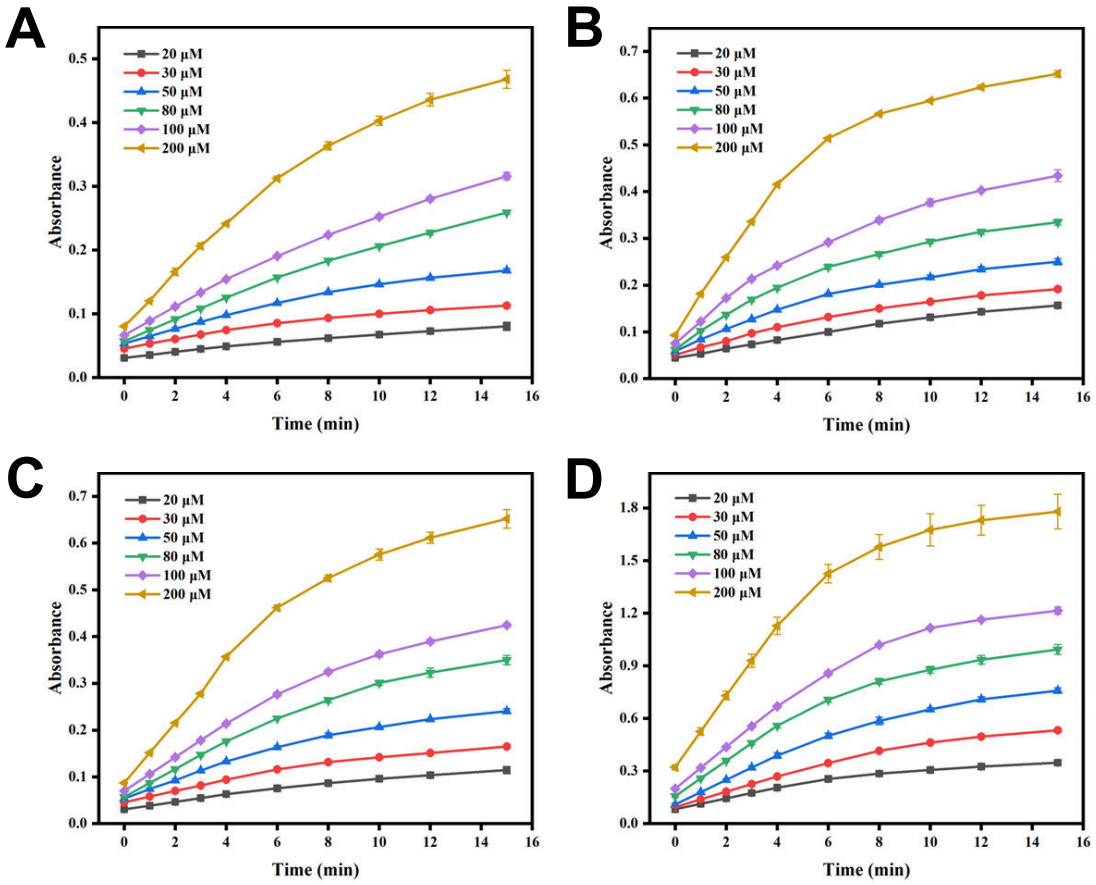

Figure S14. Absorbance changes with time at different concentrations of substrate for (A) MOF-808, (B) MOF-808/Apt, (C) MOF-808-NH_2 and (D) MOF-808-Apt in 1.5 mM NEM buffer at pH 9.0 and 37°C.

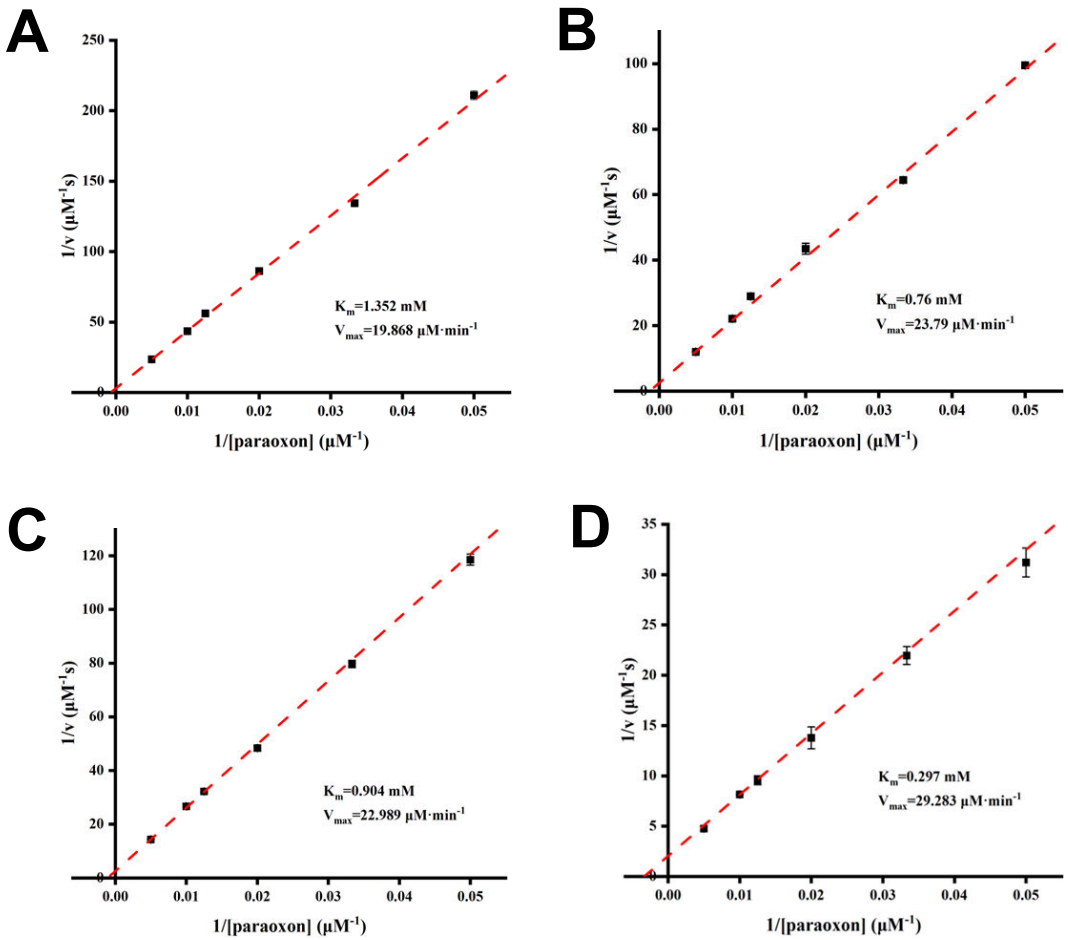

Figure S15. Double reciprocal plots of activity of (A) MOF-808, (B) MOF-808/Apt, (C) MOF-808-NH_2 and (D) MOF-808-Apt.

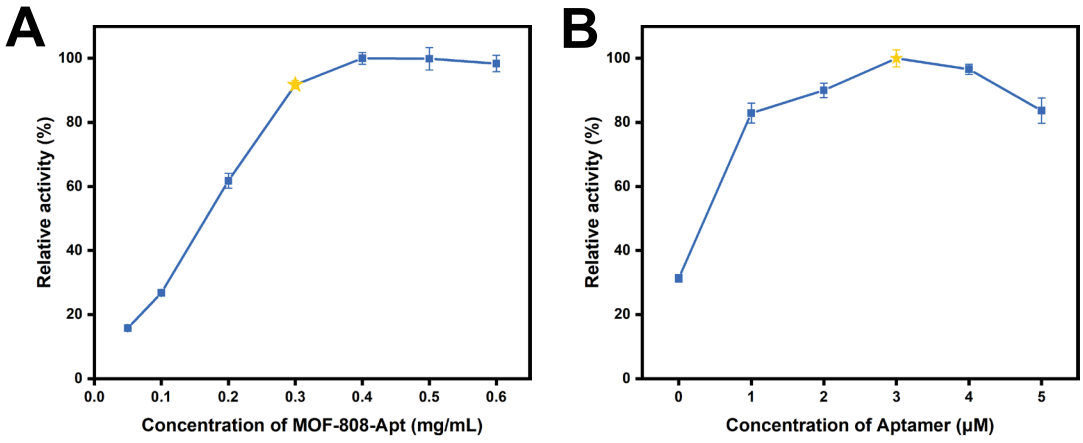

Figure S16. The catalytic ability of MOF-808-NH_2 and MOF-808-Apt on Paraoxon under different (A) concentration of MOF-808-Apt and (B) concentration of aptamers.

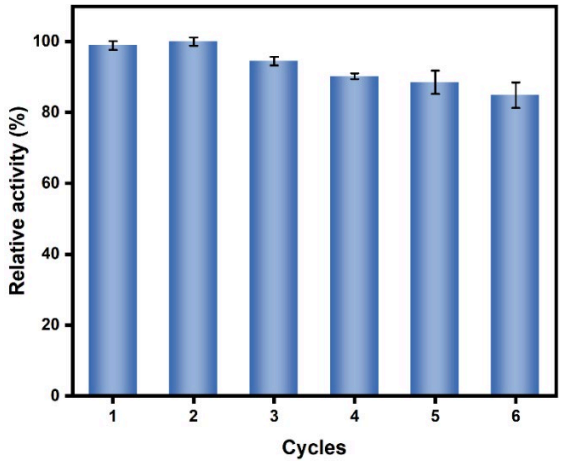

Figure S17. The catalytic activity of recycled MOF-808-Apt.

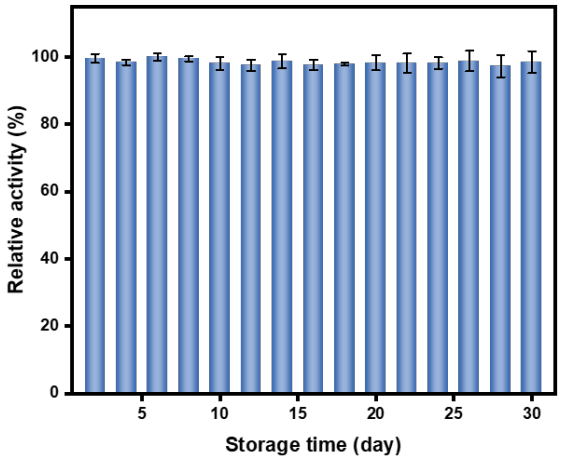

Figure S18. Long-term stability of MOF-808-Apt.

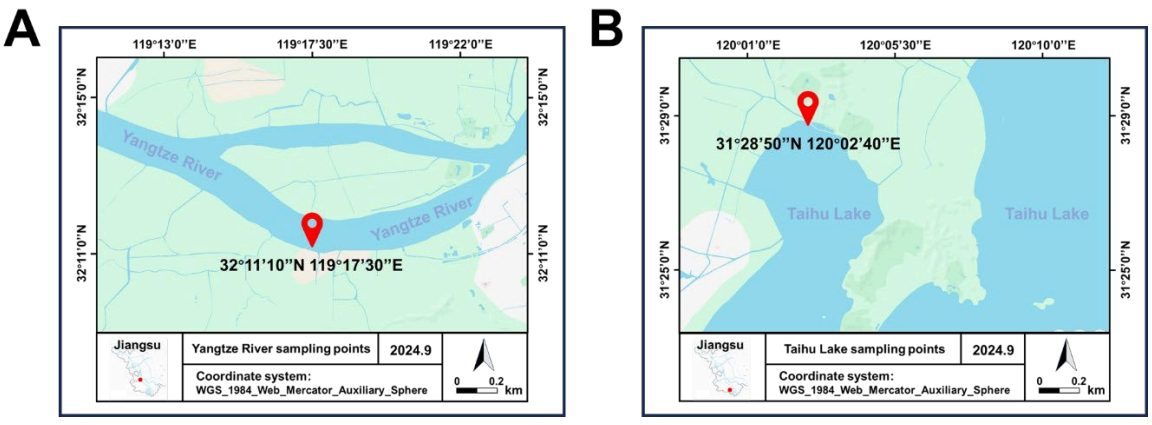

Figure S19. Sampling sites in (A) Yangtze River and (B) Taihu Lake.

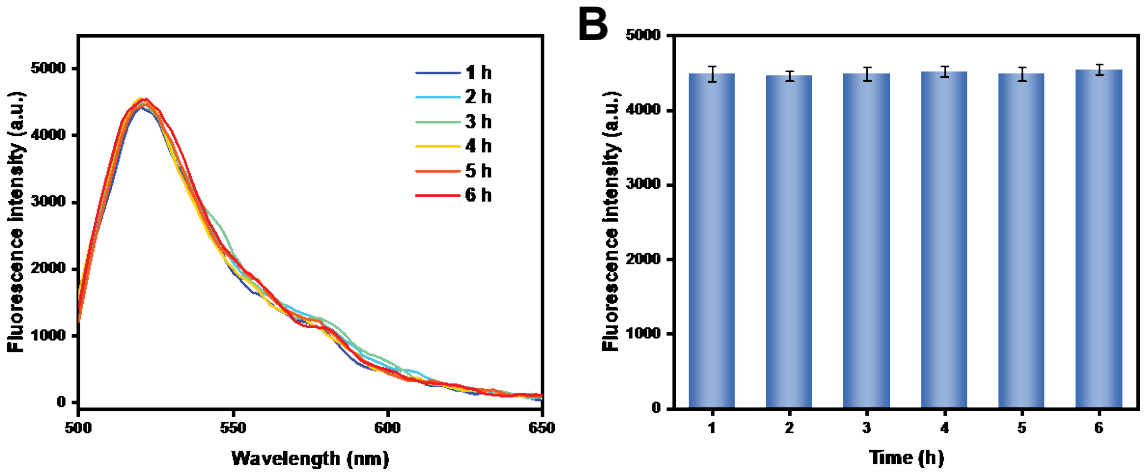

Figure S20. (A) Fluorescence curves after the fluorophore of MB activated within 6 h. (B) Long-term stability of fluorophore of MB.

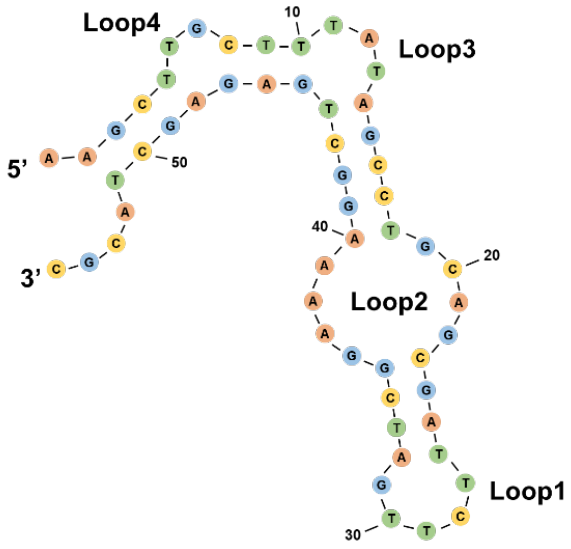

Figure S21. The secondary structure simulation of the broad-spectrum aptamer of organophosphorus pesticides.

Table S1. DNA sequences used in the experiment.

DNA	Sequence (5′–3′)
Aptamer	AAGCTTGCTTTATAGCCTGCAGCGATTCTTGATCGG AAAAGGCTGAGAGCTACGC
3′C7 Aptamer	AAGCTTGCTTTATAGCCTGCAGCGATTCTTGATCGG AAAAGGCTGAGAGCTACGC-$(CH_2)_7$-NH_2
3′C7 Poly(A)	AAAAAAAAAAAAAAAAAAAAAAAAAAAAAAAAAA AAAAAAAAAAAAAAAAAAAA-$(CH_2)_7$-NH_2
3′C7 Poly(T)	TTTTTTTTTTTTTTTTTTTTTTTTTTTTTTTTTTTTTT TTTTTTTTTTTTTT-$(CH_2)_7$-NH_2
3′C7 Poly(C)	CCCCCCCCCCCCCCCCCCCCCCCCCCCCCCCCCCCCCC CCCCCCCCCCCCCCCCCC-$(CH_2)_7$-NH_2
3′C7 Random chains	CCTAGGGCTTTATAGCAGTACTATGCGAGGTCGATG AAACTGCTGAGCTAGACGC-$(CH_2)_7$-NH_2
molecular beacon (MB)	FAM-CTGCACAAGAATCGCTGCAG-Dabcyl

Table S2. Comparison of the reported nanozymes with phosphatase-like activity.

Catalyst	Substrate	Tem. (°C)	Time (min)	Km (mM)	V_{max} μM min^{-1}	Ref.
CeO_2 NPs (10 mg/mL)	Paraoxon	75	60	--	--	Sun et al. 2021
Co_3O_4/rGO (6 mg/mL)	Paraoxon	60	20	0.083	20	Wang et al. 2017
VE CeO_2 (2.5 mg/mL) in the presence of histidine	Paraoxon	45	25	15.78	1560	Vernekar et al. 2016
Polymercbead-GOs (with Zn^{2+}) (2 mg/mL)	Paraoxon	25	360	13.5	14	Ma et al. 2017

CeO_2@NC (0.5 mg/mL)	Paraoxon	37	10	0.75	7.2	Gao et al. 2023
MOF-808				1.352	19.868	
MOF-808-NH_2				0.904	22.989	
MOF-808/Apt	**Paraoxon**	**37**	**6**	**0.76**	**23.79**	**This work**
MOF-808-Apt (0.3 mg/mL)				**0.297**	**29.283**	

Table S3. Comparison of nanozyme-mediated bioassays for paraoxon detection.

Material	Detection mode	Linear range	LOD	Ref.
Poly (TTBO)/AgNWs/BChE	Electrochemistry	0.5-8 μM 10-120 μM	0.212 μM	Turan et al. 2016
CeO_2-modified GCE	Electrochemistry	0.1-100 μM	0.06 μM	Sun et al. 2021
CeO_2 and CDs	Fluorometry	1.125-26.25 μM	0.375 μM	Chen et al. 2019
TPE-peptide probe	Fluorometry	0.6-100 μM	0.61 μM	Wang et al. 2020
Zr-TCPE AIEzyme	Fluorometry	0.82-80.7 μM	0.234 μM	Zhu et al. 2025
Zr-TCPE AIEzyme	Colorimetry	0.82-157.99 μM	0.264 μM	Zhu et al. 2025
CeO_2	Colorimetry	0.42-42 μM	0.42 μM	Wei et al. 2019
Co_3O_4/rGO	Colorimetry	8-140 μM	0.80 μM	Wang et al. 2017
CeO_2@NC	Colorimetry	3-100 μM	---	Gai et al. 2023
MOF-808-Apt	**Colorimetry**	**0.6-300 μM**	**0.18 μM**	**This work**

Table S4. Water quality monitoring data of the Yangtze River sampling points and Taihu Lake sampling points.

Test item	Test result data	
	Yangtze River Sampling point	Taihu Lake Sampling point
Temperature (°C)	24.2	21.6
pH	8.0	8.0
Dissolved oxygen (mg/L)	6.9	8.8
Permanganate index (COD_{Mn}) (mg/L)	3.0	2.5
Ammonia nitrogen (mg/L)	0.12	0.04
Total phosphorus (mg/L)	0.06	0.06
Chemical oxygen demand (COD_{Cr}) (mg/L)	12.0	13.0
Five-day biochemical oxygen demand (BOD_5) (mg/L)	1.8	2.1

Table S5. Recoveries of paraoxon detection in real samples.

Water samples	No.	Paraoxon added (μM)	Paraoxon detected (μM)	Recovery (%)	RSD (%)
Yangtze River water	1	5	4.8	96	3.1
	2	50	51.9	103.8	2.9
	3	300	297.6	99.2	3.9
Taihu Lake water	1	5	4.9	98	2.2
	2	50	50.9	101.8	3.6
	3	300	295.9	98.6	4.1

https://dspace.org/

Targeted enrichment of nucleic acid bionic arms enhances the hydrolysis activity of nanozymes for degradation and real-time monitoring of organophosphorus pesticides in water

Zhou, Jialong; Xiong, Dinghui; Zhang, Hu; Xiao, Jiaxuan; Huang, Rui ...

2025-01-28
American Chemical Society
https://doi.org/10.1021/acs.est.4c13849
Zhou J, Xiong D, Zhang H, et al., (2025) Targeted enrichment of nucleic acid bionic arms enhances the hydrolysis activity of nanozymes for degradation and real-time monitoring of organophosphorus pesticides in water. Environmental Science & Technology, Volume 59, Issue 3, January 2025, pp. 1844-1853

Downloaded from a DSpace repository. https://dspace.org/